Journal of African Earth Sciences 232 (2025) 105816

Contents lists available at ScienceDirect

Journal of African Earth Sciences

journal homepage: www.elsevier.com/locate/jafrearsci

Machine learning-based lithological mapping and mineral prospecting using hyperspectral and multispectral remote sensing in Wadi Halfa, north Sudan

Abazar M.A. Daoud [a,b,*], Ali Shebl [a,c], Mutwakil Nafi [d,e], Abdelmajeed A. Elrasheed [f,g], Árpád Csámer [a,h], Péter Rózsa [a]

[a] Department of Mineralogy and Geology, University of Debrecen, Egyetem Tér 1, 4032, Hungary
[b] Engineering Geology Department, Faculty of Earth Sciences, Red Sea University, Sudan
[c] Department of Geology, Tanta University, 31527, Tanta, Egypt
[d] Faculty of Minerals and Petroleum, International University of Africa, Khartoum, Sudan
[e] Department of Petroleum Engineering, Faculty of Engineering, International University of East Africa, Kampala, Uganda
[f] Department of Physical Geography and Geoinformatics, University of Debrecen, Hungary
[g] Geology Department, Faculty of Science, University of Khartoum, Sudan
[h] Cosmochemistry and Cosmic Methods Research Group, University of Debrecen, Debrecen, 4032, Hungary

ARTICLE INFO

Handling Editor: M Mapeo

Keywords:
Support vector machine
Artificial neural network
Mahalanobis
Iron ore
Barite
Economic reserves

ABSTRACT

At present, the global demand for mineral resources is critical, leading nations to focus on exploration. Remote sensing is a cost-effective tool, especially in harsh terrains. This study conducted lithological mapping in Wadi Halfa, North Sudan, using algorithm-based remote sensing, field observations, and petrographical analysis to detect iron ore and barite deposits. Multisensor optical datasets (L9, L8, and S2) were integrated to effectively delineate the lithological units. In addition, PRISMA hyperspectral data, with its detailed spectral signatures, improved spatial distribution patterns of barite and iron oxides across the study area. Image processing techniques (false colour composites, principal component analysis, minimum noise friction, band ratios) detected hydroxyl-bearing minerals, ferric, and ferrous oxides. Support Vector Machine (SVM), Artificial Neural Network (ANN), and Mahalanobis Distance Classifier (MDC) achieved overall accuracies of 95.51 %, 94.59 %, and 98.99 %, respectively. The study helped interpret the spatial relationship between barite and iron oxides. Four types of iron ore with more than three distinct layers were identified, including (a) oolitic ironstone, (b) ferruginous sandstone, (c) ferruginous ironstone, and (d) Banded Iron Formation (BIF) during field investigations, petrographic examinations, and chemical analysis validated remote sensing findings, revealing iron ore (62.7 % Fe) and barite (63.9 % Ba) concentrations. An economic assessment confirmed the presence of economic reserves suitable for exploitation. This research is recommended for broader application, particularly in machine learning for delineating iron ore and barite deposits in complex sedimentary sequences. The realization of machine learning algorithms emphasizes their potential to enhance lithological mapping in sedimentary sequences, suggesting a promising direction for future research.

1. Introduction

Iron ores and barite ($BaSO_4$), as critical minerals, play a vital role in various industries, contributing significantly to the global economy (Hayes and McCullough, 2018; Penaloza et al., 2023). Their presence often indicates the mineralization of variable metallic deposits, including gold, copper, lead, and manganese (Abdelrahman et al., 2024; Abu-Fatima et al., 2021; Li et al., 2021). The integration of remote sensing, field observations, and laboratory analysis is therefore essential for detecting these minerals, suggesting a strategic approach to uncover

* Corresponding author. Department of Mineralogy and Geology, University of Debrecen, Egyetem Tér 1, 4032, Hungary
E-mail addresses: Abazar.daoud@science.unideb.hu, daoudabazar@gmail.com (A.M.A. Daoud), ali.shebl@science.tanta.edu.eg (A. Shebl), mutwakilnafi@gmail.com, mutwakil.nafi@iuea.ac.ug (M. Nafi), mageedelrasheed25@gmail.com (A.A. Elrasheed), csamera@unideb.hu (Á. Csámer), rozsa.peter@science.unideb.hu (P. Rózsa).

https://doi.org/10.1016/j.jafrearsci.2025.105816
Received 28 February 2025; Received in revised form 11 August 2025; Accepted 11 August 2025
Available online 14 August 2025
1464-343X/© 2025 The Authors. Published by Elsevier Ltd. This is an open access article under the CC BY license (http://creativecommons.org/licenses/by/4.0/).

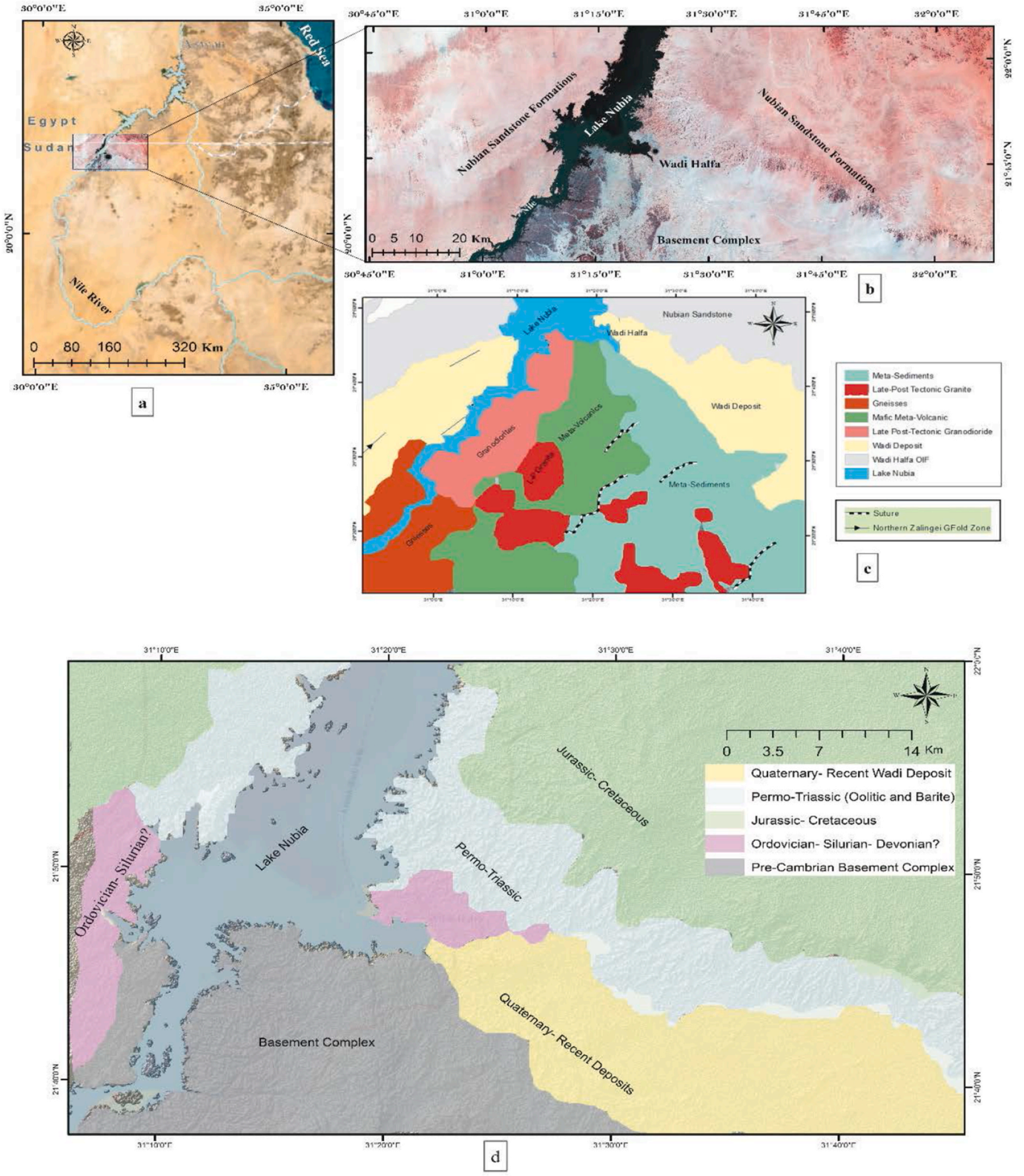


Fig. 1. (a) General location map highlighting the study area; (b) RGB satellite image (7-5-3) illustrating major geological and geomorphological features; (c) Simplified geological sketch map of the basement complex south of Wadi Halfa, redrawn and modified from (Stern et al., 1994); (d) Detailed geological map of the WHOI Formation.

additional metallic and industrial mineral resources.

The application of remote sensing for lithological mapping is essential for mineral explorations due to its simplicity and cost-effectiveness, especially in arid and semi-arid regions. Remote sensing allows geologists to collect detailed surface data quickly, supporting large-scale geological surveys targeted at detecting mineral deposits (Abdelkareem and Al-Arifi, 2021; Shebl and Hamdy, 2023; Van der Meer et al., 2014). Previous studies in Sudan have primarily focused on using

Table 1
Spectral band ratios and indices are used for detecting specific mineral indicators from L9, L8, S2 imagery.

Mineral Indications	L 8 & 9	S2	References
Iron sulfate index	(2/1–5/4)	11/2	(Rockwell et al., 2021; Bedini, 2017)
Ferric oxides	(4/3) or (4/2)	4/3	(van der Meer et al., 2012; Van der Meer et al., 2014; van der Werff and van der Meer, 2015)
Ferrous iron oxide	(7/5 + 4/3)	(12/8A + 3/4)	
Hydroxyl bearing minerals	6/7	11/12	Pour et al. (2019)
Clays and sulfate	(6/7- 5/4)	–	Rockwell et al. (2021)

hyperspectral and multispectral remote sensing to detect metallic minerals, largely ignoring significant economic industrial minerals such as iron ore and barite (Elsayed Zeinelabdein et al., 2020; Elsheikh et al., 2014; Mohamed Taha et al., 2023). In contrast, a recent study conducted by (Daoud et al., 2025) focused on delineating barite deposits of hydrothermal origin within the Red Sea Hills.

Algorithms, such as Neural Networks (NN), Support Vector Machine (SVM), Random Forest (RF), Extreme Gradient Boosting (XGBoost), and Anomaly Detection (AD) have been known to be effective in different geological fields, including petroleum geology, where they have been successfully used to optimize geothermal reservoir modelling (Ullah et al., 2024), for lithological mapping and mineral explorations, machine learning algorithms (MLA) conducive to strong adaptable results in classifying and detecting mineral deposits in different complex geological terrains (Costa et al., 2020; Mahboob et al., 2024; Nwaila et al., 2022; Shebl et al., 2024; Shirmard et al., 2022). The present study applies these techniques in multiscale integrated hyperspectral and multispectral remote sensing for detecting and mapping iron ore and barite deposits in Wadi Halfa as the first study to use these algorithms for the detection and delineation of iron anomalies within sedimentary sequences.

In recent periods, the Wadi Halfa region in northern Sudan has undergone substantial urban development, primarily due to its strategic location near the Egyptian border, which provides a higher degree of safety compared to other areas in Sudan due to war conditions. As a result, many large corporations and manufacturing companies have moved their operations to Wadi Halfa. This region's unique geological resources, which include a variety of metallic and industrial minerals such as gold, copper, iron ore, and barite, as well as construction building materials like gravel, sand, silt, and various clays, are of additional industrial interest. Thus, this study aims to investigate and delineate the iron ore and barite deposits in the Wadi Halfa region using an innovative approach that combines mega-scale remote sensing techniques followed by machine learning algorithms with micro-scale petrographic analyses. Moreover, this research pioneers the integration of hyperspectral PRISMA satellite imagery with multispectral data from Landsat 8, Landsat 9, and Sentinel-2 (L8, L9, and S2) to explore iron ore and barite deposits. This methodology has led to the discovery of new occurrences of sedimentary iron ore and barite deposits around the Wadi Halfa region in northern Sudan.

Previous studies have primarily focused on metallic mineral exploration in basement terrains, often overlooking industrial minerals such as barite and iron ore in sedimentary sequences. The current study is the first to apply remote sensing and advanced machine learning algorithms (ANN and SVM) for multi-sensor integration of hyperspectral and multispectral datasets to detect and map these minerals in the Wadi Halfa region, specifically within sedimentary sequences.

2. Study area & geology

Wadi Halfa is a city in the Northern State of Sudan on the shores of Lake Nubia near the border with Egypt. This region has significant historical value as it served as the cradle of the Nubian civilization, one

Table 2
Distribution of training and testing samples used in supervised classification. The dataset includes representative point-based-pixels for each lithological class to ensure balanced model performance. Percentages reflect the proportion of testing pixels relative to the total per class.

Class	Training Pixels	Testing Pixels	Testing proportions (%)
Ironstone	829	245	28.11
Sandstone	893	256	29.18
Quaternary and recent deposits	858	235	28.54
Lake Nubia	857	243	29.25

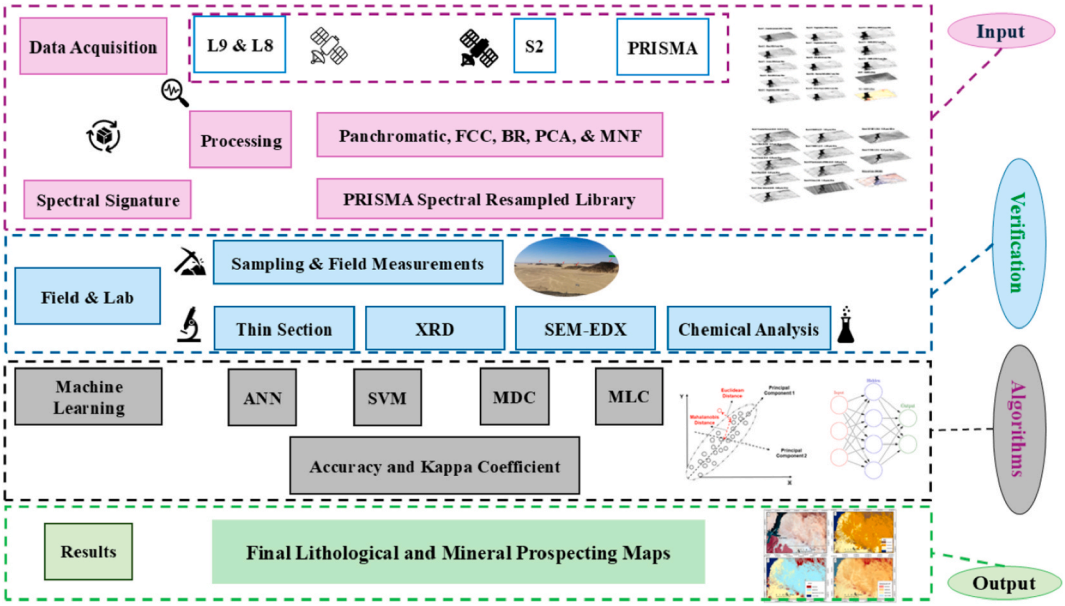


Fig. 2. Flowchart illustrating the methodological framework employed in this study.

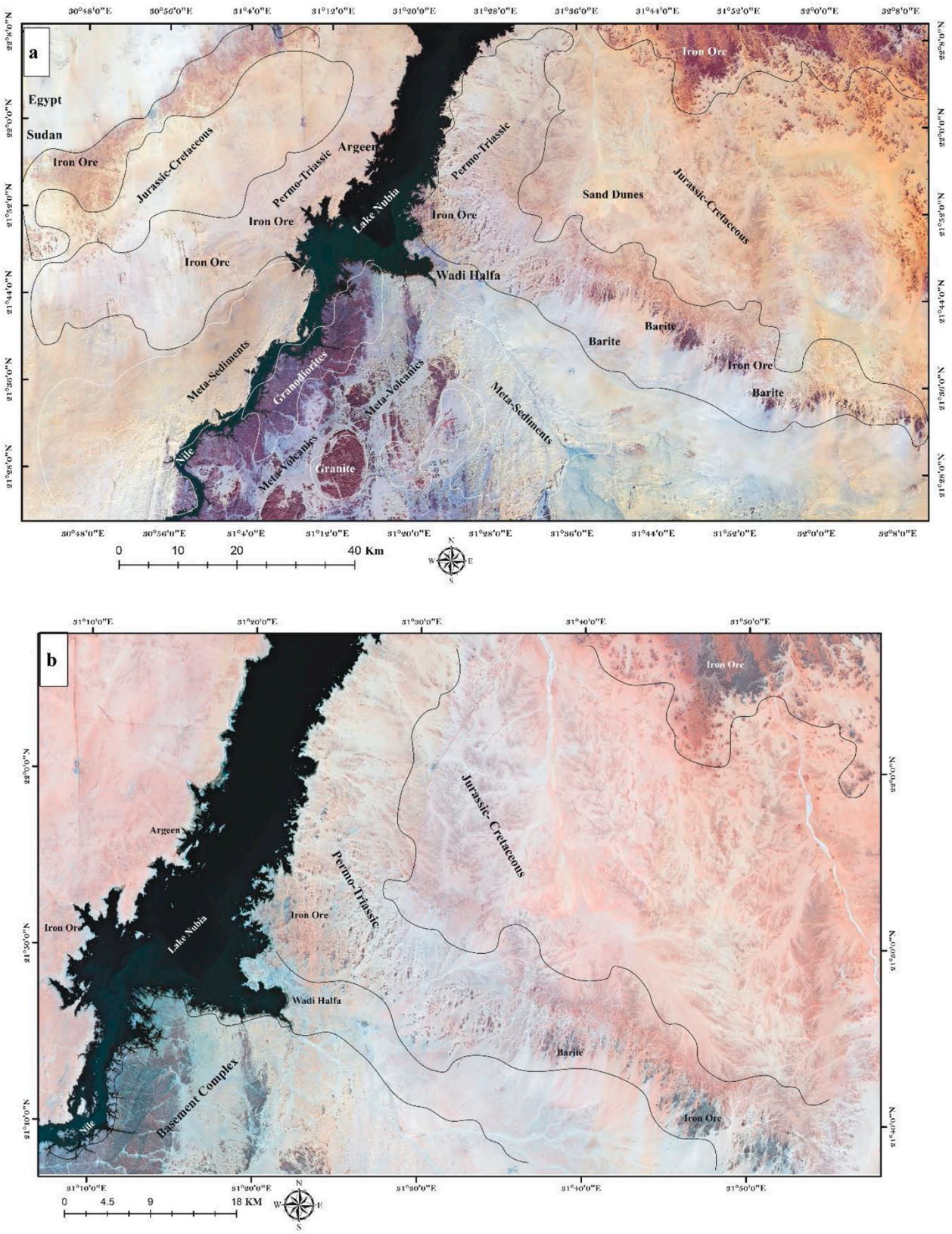


Fig. 3. (a) L9 colour composite (R6-G3-B1); (b) S2 (R5-G2-B1) showing the major rock units in the study area; basement complex in the south and the Nubian Sandstone with different types of iron ore in the north.

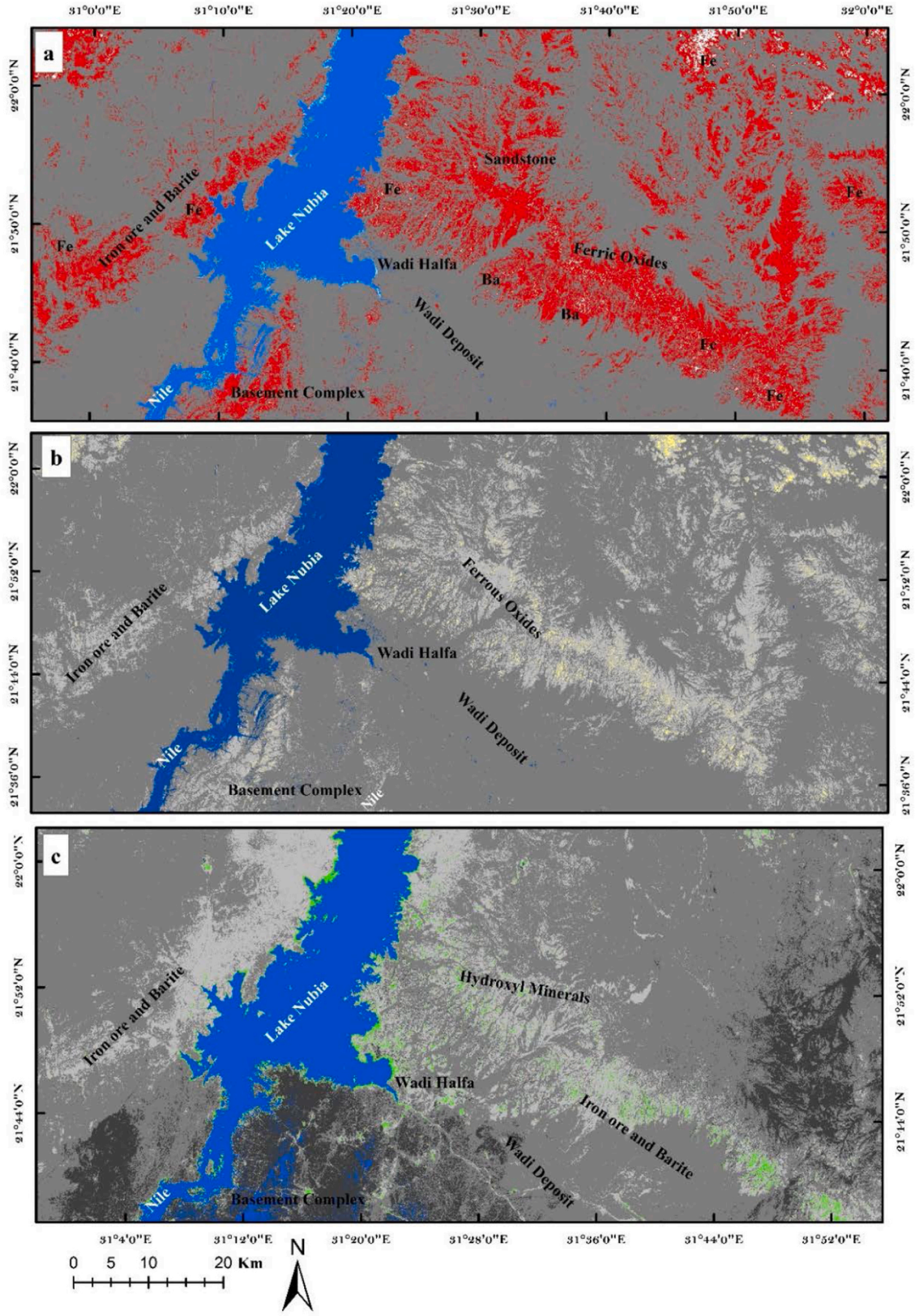


Fig. 4. Landsat 9 ratios of (a) bands (4/3) displaying the high concentration of ferric oxides-bearing rocks in red colour; (b) silica and barite alteration (7/5) in yellow colour; (c) Al-OH alteration using bands (6/7) as appear in green colour.

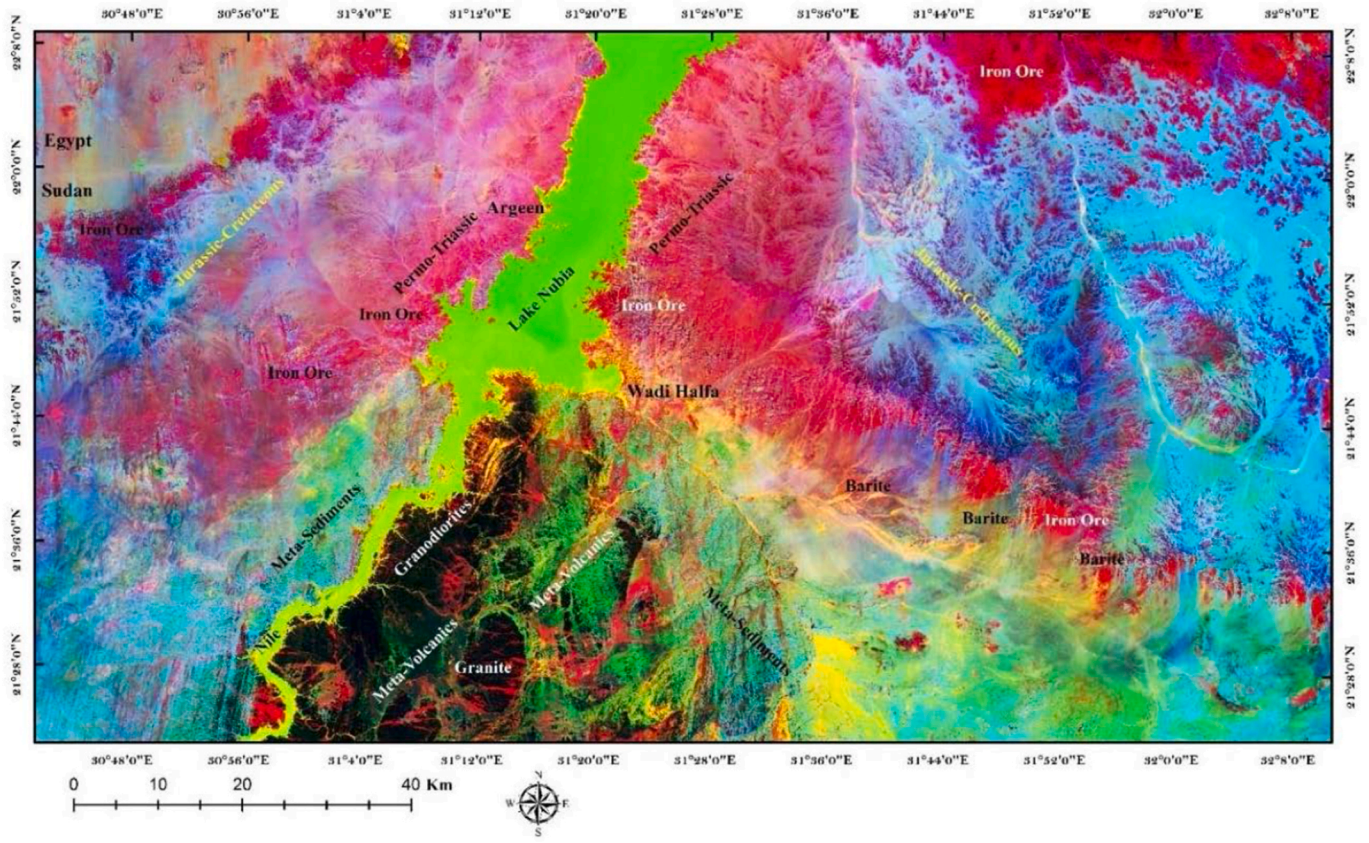


Fig. 5. False colour composite of (R4/2-G6/5-G7/6) in L8 showing the distribution of basement complex in the south and the sandstone in the north with iron oxides and barite (appears as Red) and Cretaceous sandstone as light blue colour that reflects the clay minerals (AL-OH) at the top of the most studied sections.

of the oldest ones in the world. Positioned as a crucial land and lake port alongside the Arab Republic of Egypt, it is accessible through a road and a river port on Lake Nasser. Furthermore, it is connected to other cities in Sudan via national roads on the east and west sides of the lake, along with a railway line extending to the capital, Khartoum (Fig. 1a).

Wadi Halfa, surrounded by the Nubian Sandstone Formation (now become meaningless from both the sedimentological and stratigraphical points of view) known as Wadi Halfa Oolitic Ironstone Formation (WHOIF) [Latitude: 21°49′N, and Longitude: 31°21′E] as illustrated in (Fig. 1b). Geologically, the study area exhibits two distinct geological rock units: the Precambrian basement complex rocks in the southern region (Stern et al., 1994) and the Late Carboniferous – Permo-Triassic – Lower Jurassic WHOIF in the northern area (Daoud et al., 2020, 2021, 2024; Nafi et al., 2015). This formation is then unconformably covered by the wadi deposit of Quaternary origin, including a mixture of materials such as gravel, sandy clays, silt, and clays (Fig. 1c).

The basement complex in northern Sudan consists of three major units: grey gneisses, metasedimentary formations, and volcano-sedimentary rocks (Vail, 1990). South of Wadi Halfa, five primary lithologies characterize the basement: a foliated gneissic terrane overlain by a less deformed supracrustal succession, mafic metavolcanic rocks, and metasedimentary and felsic metavolcanic rocks. These units are intruded by syntectonic granodiorites and post-tectonic alkali granites (Stern et al., 1994) (see Fig. 1c). The high-grade polymetamorphic and granitoid basement west of the Nile belongs to the East Saharan Craton and likely represents a pre-Pan-African tectonic entity (Abdelsalam et al., 2002; Lemdjou et al., 2022; Schandelmeier et al., 1987).

The WHOI Formation comprises different lithofacies, including fluvial, glacial, fluvioglacial, and shallow marine sediments. These facies include different sandstones (trough and planar cross-bedded, horizontally stratified, rippled), fine and massive mudstones, shallow marine sandstones, barite, and oolitic ironstone facies (Fig. 1d).

3. Data and methodology

3.1. Remote sensing data

Multispectral remote sensing Landsat 8 & 9 (11 bands) and Sentinel 2 (12 bands) were downloaded from the US Geological Survey site (https://www.earthexplorer.usgs.gov) and (https://dataspace.copernicus.eu), respectively, with a spectral resolution band covering the visible, near-infrared, and shortwave infrared regions. In addition to utilizing these multispectral sensors, our study took a step forward by incorporating PRISMA hyperspectral data to enhance the distribution patterns of barite and iron oxides within the study area. PRISMA (PRecursore IperSpettrale della Missione Applicativa) is an advanced hyperspectral satellite that provides 242 bands, covering visible and shortwave infrared spectral regions.

3.2. Image processing techniques

False colour composites (FCCs) were generated by assigning specific spectral bands to RGB channels to visually enhance geological features and support mineral exploration (Askari et al., 2018; Eldosouky et al., 2021; Jain, 2021; Pour et al., 2019; Shebl and Hamdy, 2023). To further enhance image interpretation, various processing techniques were applied, including band rationing (BR), principal component analysis (PCA), and raster calculations (band math), following established mineral indices (summarized in Table 1).

The band ratio technique was particularly effective for identifying and delineating iron ore and barite deposits (Abay et al., 2022; Ninomiya and Fu, 2019; Rockwell et al., 2021; van der Werff and van der

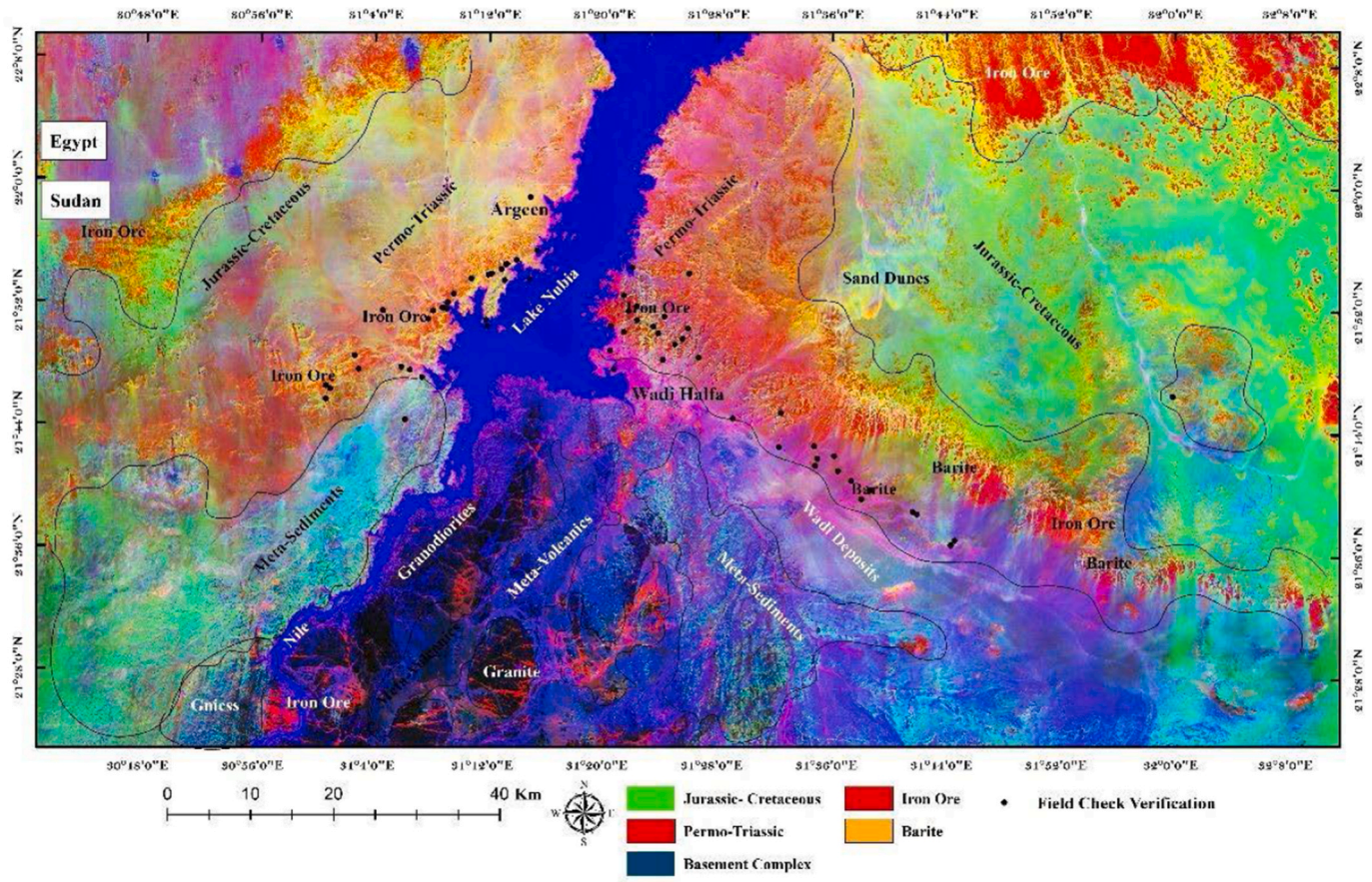


Fig. 6. False colour composite using L9 showing the distribution of Permo-Triassic sandstone containing iron ores and barite (Red) and Jurassic-Cretaceous sandstone (Green).

Meer, 2015). Feature-oriented PCA improved lithological discrimination and revealed the spatial distribution of ferric, ferrous, and hydroxyl-bearing minerals (Jain, 2021; Su et al., 2023). Finally, lithological mapping and mineral delineation were refined using both iso-cluster unsupervised and supervised (maximum likelihood) classification algorithms, as illustrated in the methodological workflow (Fig. 2).

3.3. Field observations & sampling

Seventy vertical lithofacies sections around the region of Wadi Halfa were carefully investigated to validate our findings from remote sensing. Fifty representative rock samples were carefully collected from different vertical lithological units and then labeled and prepared for the petrographic analysis.

3.4. Laboratory analyses

To determine the mineral composition of the representative selected samples, a series of advanced laboratory analyses, including thin-section microscopic studies and scanning electron microscopy (SEM) coupled with energy dispersive X-ray spectroscopy (EDX) were conducted at the Electron Microscope Unit, Faculty of Sciences Alexandria University, Egypt using a JEOL JSM-5300 and equipped with an energy dispersive X-ray micro analyzer SEM-EDAX (OXFORD).

Detailed chemical analyses using X-ray fluorescence (XRF) were also performed to ascertain the chemical composition of the iron ore samples in the Geological Research Authority of Sudan (GRAS) and OMAC Laboratory Ltd., with a Phillips PW1480 automated spectrometer.

3.5. Machine learning based-classification and anomaly detection

Several supervised classification algorithms were applied to the L9 imagery, enhanced to a 15 × 15-m pixel resolution using panchromatic sharpening, to accurately delineate lithological units and identify mineralized zones. Support Vector Machines (SVMs) were employed due to their ability to find an optimal hyperplane for class separation in high-dimensional spectral space, making them effective for lithological classification, particularly with small sample sizes and complex spectral relationships (El-Omairi et al., 2025; Evans, 1988; Petropoulos et al., 2012; Rajan Girija and Mayappan, 2019; Shebl et al., 2022; Ullah et al., 2025). Artificial Neural Networks (ANNs) were also utilized to account for nonlinear spectral variations and enhance lithological classification accuracy (Ullah et al., 2025; Vapnik, 1995; Wilamowski, 2009). Additionally, the Mahalanobis Distance Classification (MDC) is widely used in lithological mapping based on the distance between each lithological rock unit (Chen et al., 2023; Sankhya A., 2018), and was applied in the present study effectively. The maximum likelihood classification (MLC) is also applied in the current study as the most common algorithm used recently for lithological mapping (Tsangaratos et al., 2025; Verbovšek and Popit, 2018; X. Zhang et al., 2007; Z. Zhang et al., 2025). Furthermore, anomaly detection played a critical role in identifying regions with high iron ore mineralization (Nwaila et al., 2022), particularly through the computation of ferric, ferrous, hydroxyl, and barite-bearing minerals, where higher ferric values indicated iron-rich anomalies. Since iron oxide minerals such as hematite and goethite exhibit strong absorption features in specific wavelengths (Doner et al., 2019; Noda and Yamaguchi, 2017; Tamehe et al., 2024; Ullah et al., 2023), these spectral indices were calculated for each pixel and incorporated as input features in the machine learning models to enhance mineral detection accuracy.

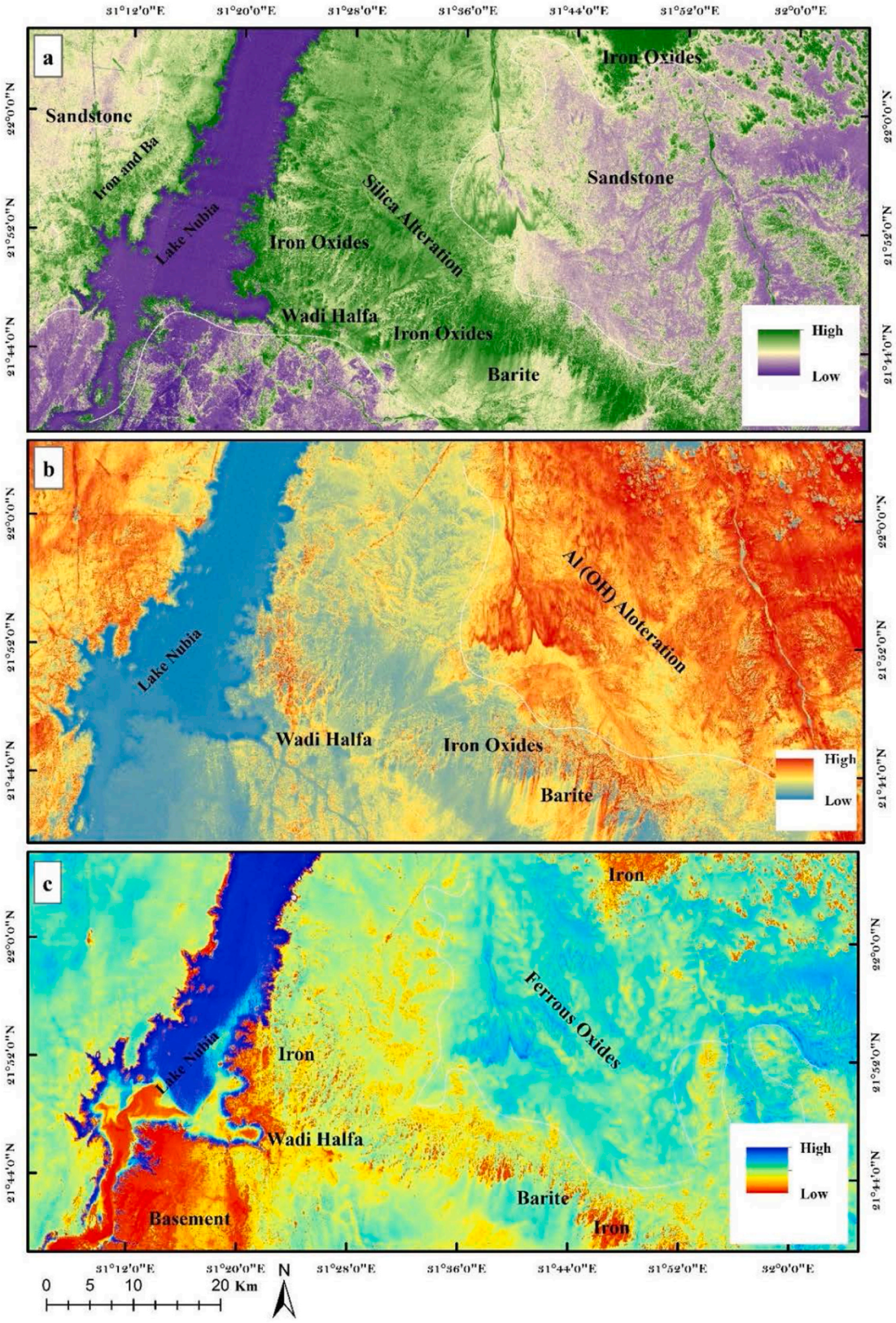


Fig. 7. Band ratios of S2, (a) hydroxyl bearing minerals (11/12) appear as green colour; (b) (4/2) showing ferric oxide appearing as dark red colour whereas the iron oxide appears as light blue; (c) (4/11) shows the ferrous oxides appearing as light blue colour.

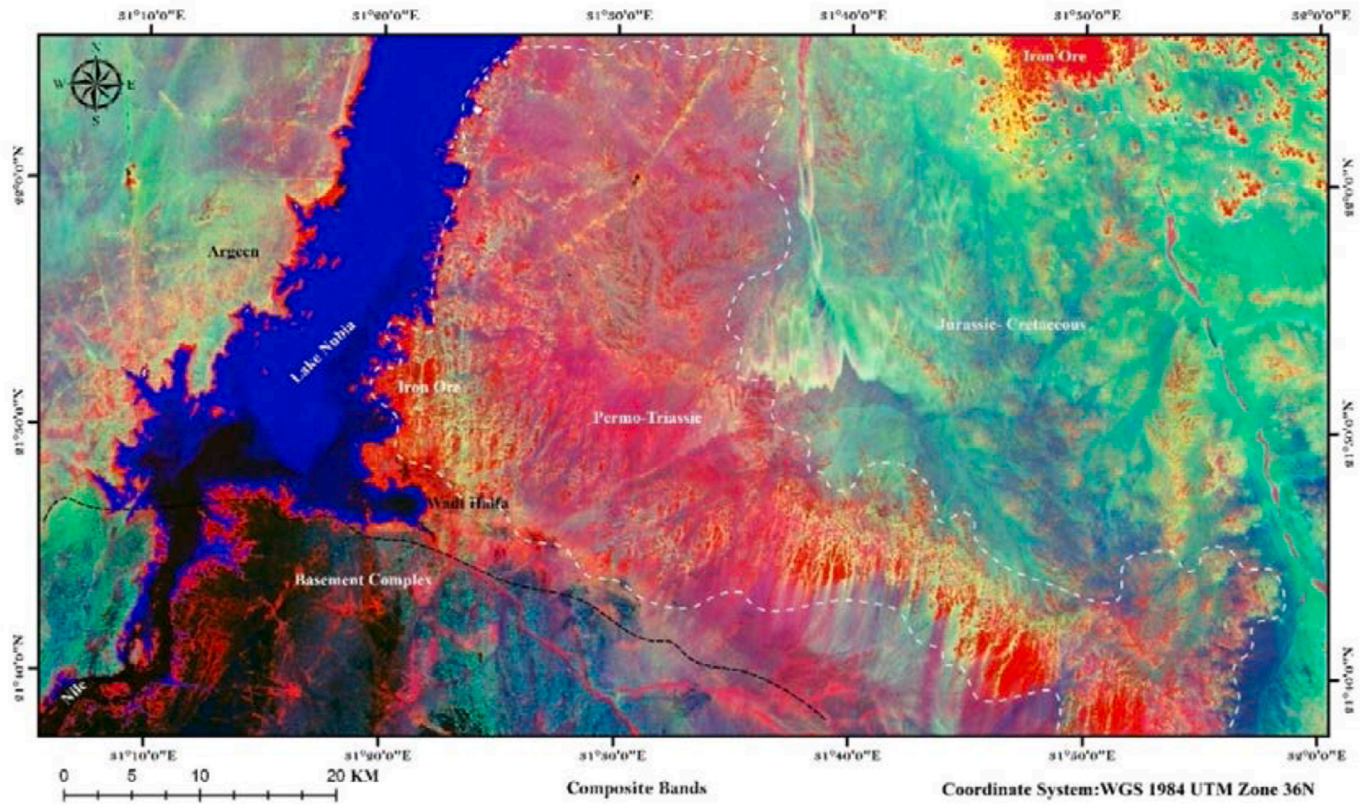


Fig. 8. False colour composite in S2 corresponds to hydroxyl (11/12), ferric oxides (4/2), and ferrous oxides (4/11) as RGB, respectively, showing the distribution of the Permo-Triassic sandstone containing iron ores and barite (Red) and Jurassic-Cretaceous sandstone (Green).

Training samples were selected based on ground truth field observations and laboratory analysis. The classification models were fine-tuned using cross-validation to maximize accuracy. Due to the presence of extensive sedimentary sequences and Lake Nubia within the study area, the lake was classified as a separate unit to minimize misclassification errors during the modeling process. Three major lithological units were identified: (1) Upper Carboniferous – Permo-Triassic to Lower Jurassic oolitic ironstone, which occurs in three distinct layers (top, middle, and lower), with the top layer being well-defined using various techniques such as FCC, BR, and PCA; (2) Quaternary and recent deposits, primarily occurring along wadis and khors; and (3) Cretaceous sandstone, which forms the dominant lithological unit in the area. Table 2 provides a detailed summary of these classified units as training and testing datasets with percentages of 70–75 % to 25–30 % of training and testing data, respectively.

The process for the advanced machine learning algorithms (ANN, SVM, MDC, MLC) was conducted using the ENVI software. For the ANN algorithm, the training process was guided by a training rate of 0.200 and a momentum value of 0.9 to enhance convergence stability. To optimize classification accuracy, the ANN logistic activation parameters were adjusted with a single hidden layer and 1000 training alterations. For the SVM algorithm, the Radial Basis Function (RBF) kernel 0.333 and a penalty parameter of 100 were applied. The classification results were validated using an independent set of field sample coordinates and previous geological maps. Performance evaluation included a confusion matrix which provides overall accuracy and the Kappa coefficient, and comparison with field data to ensure consistency between classified mineral zones and ground-truth observations.

4. Results

4.1. Remote sensing

4.1.1. False colour composite & band ratios

FCCs of L9 (R6-G3-B1) and S2 (R5-G2-B1) show relevant major geological features within the study area. For instance, the basement complex rock in the south appears as reddish, brownish to dark brownish colour, while the sedimentary rock in the north parts reflects a yellowish and light brown colour for iron ore deposits, as shown in Fig. 3a and b, respectively.

Utilizing L9, 8 data and previous studies summarized in Table 1, dividing bands (6/5), (7/5), and (6/7) significantly identifying the pattern of ferric bearing rocks displays the iron ore with high values in dark red colour (Fig. 4a); ferrous-minerals bearing rocks display light yellow colour as shown in Fig. 4b; and displayed the iron ore and barite deposits with hydroxyl-bearing minerals in green colour (Fig. 4c). The composite of R4/2-G5/6-B6/7 proves valuable in mapping ferric, ferrous, and hydroxyl-bearing minerals, as it capitalizes on their absorption characteristics in the blue region, where they exhibit high reflectance in the red region. This representation likely utilizes the red, green, and blue channels of the RGB colour model to highlight and distinguish these specific mineral types (Figs. 5 and 6).

Employing S2 data, dividing bands (11/12) help us to discriminate iron ore and barite from the surrounding rocks as in Fig. 7a for Permo-Triassic sandstone with a high content of iron oxides and barite similarly to hydroxyl-bearing minerals (Al-OH). Ironstone in the study area typically exhibits higher reflectance in the short-wave infrared bands (SWIR1 and SWIR2) compared to the VNIR and NIR bands (Salem and El Gammal, 2015; Velasco et al., 2005).

Ferric oxides (Fe_2O_3) exhibit significant absorption characteristics, as indicated by the division of bands (4/3) as shown in Fig. 7b, which indicates a high content of Fe_2O_3 in Jurassic-Cretaceous sandstone. In

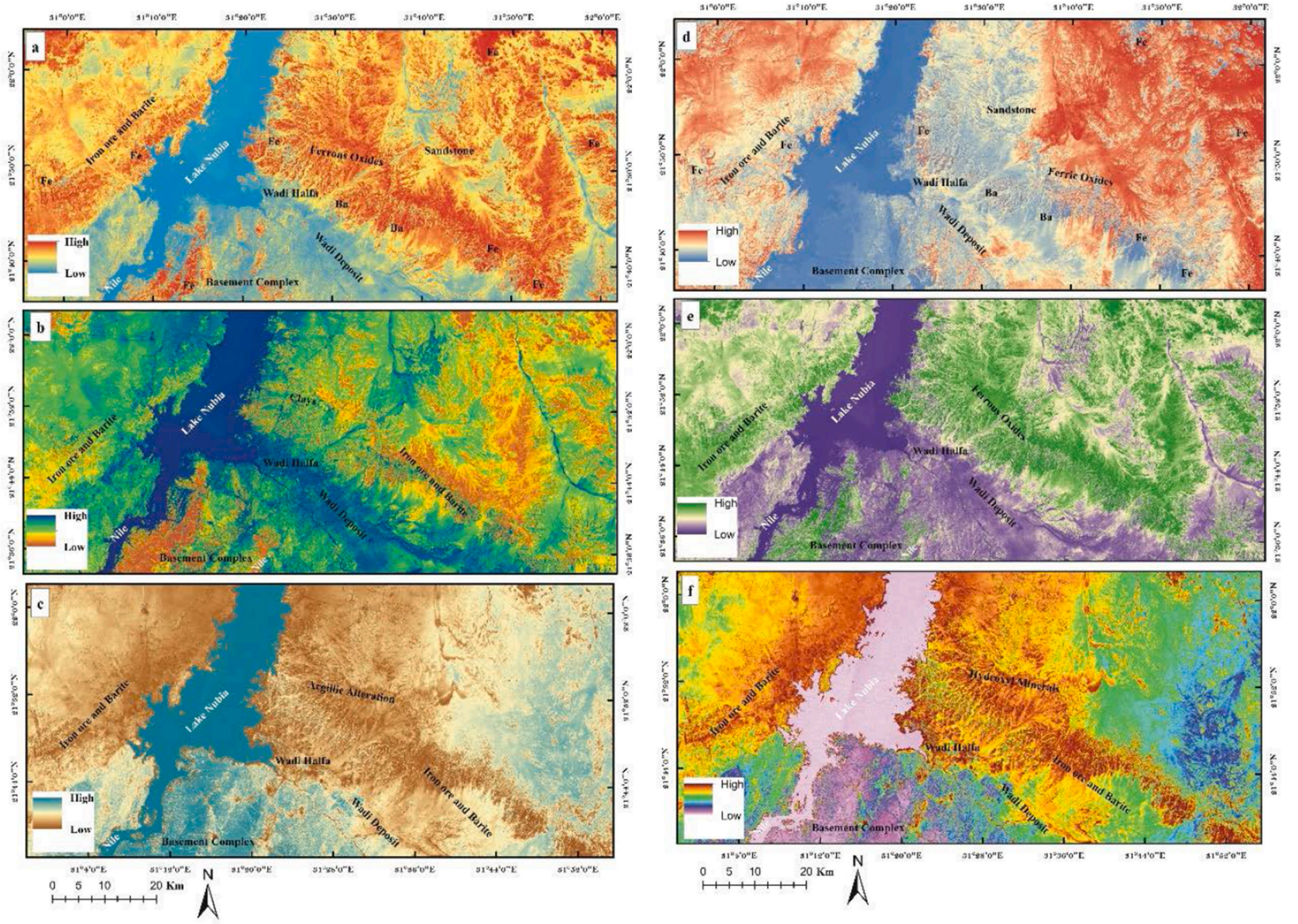


Fig. 9. (a) silica (11/12) in S2 (b) Al-OH (e.g., kaolinite, muscovite); (6/7) in L9; (c) ferrous minerals (4/6); (d) all iron oxides (4/2); (e) ferrous silicates (12/11) in S2; (f) carbonates (12/2) in S2.

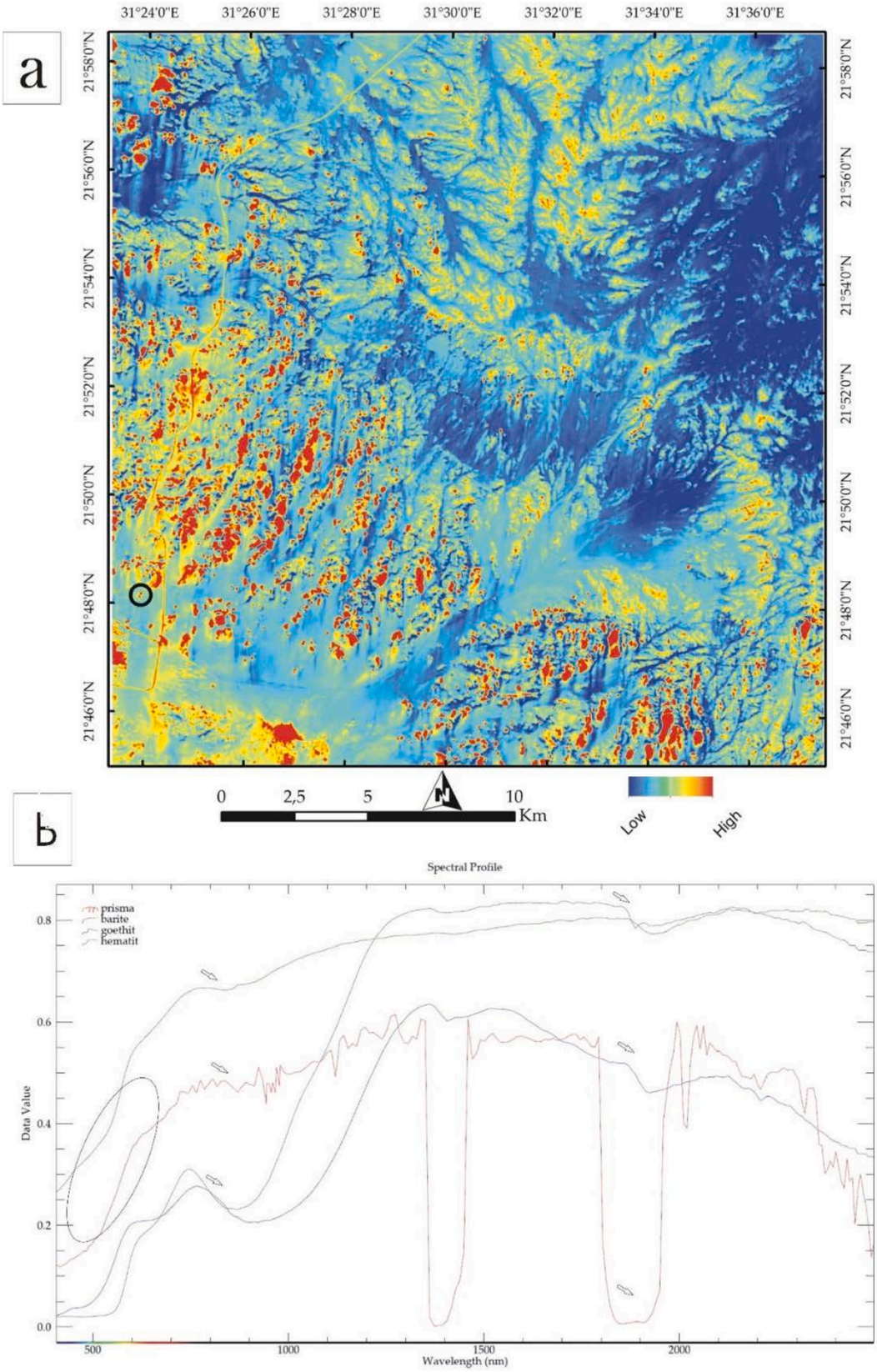


Fig. 10. (a) PC1 of PRISMA data showing iron oxide-bearing rocks and barite deposits in red colour; (b) Spectral profile of VNIR-SWIR showing the similarity between the signatures of barite, hematite, and goethite with the spectral characteristics of the detected red pixels within the study area (oval and arrows).



Fig. 11. Field photographs showing (a) a general view of iron ore deposits with three different layers (red arrows); (b) ferruginous ironstone; (c) oolitic ironstone; (d) ferruginous iron ore concretion; and (e) ferruginous sandstone.

contrast, ferrous iron exhibits absorption by dividing bands (4/11) (Fig. 7c). The ratio (R11/12-G4/2-B4/11) for hydroxyl, ferric, and ferrous oxides, respectively, in S2 is used in the present study for mapping iron ores and barite deposits, as shown in Fig. 8.

In addition, various BRs related to key alteration minerals such as silica (11/12) in S2 (Fig. 9a), Al-OH (e.g., kaolinite, muscovite) (6/7) in L9 (see Fig. 9b), ferrous minerals (4/6 in Fig. 9c), all iron oxides (Fe^{+2} and Fe^{+3}) (4/2) in both L9 and S2 (Fig. 9d), ferrous silicates (12/11) in S2 (Fig. 9e), and carbonates were applied to S2 (12/2) (Fig. 12f) in order to enhance the discrimination of lithological units and associated mineralogical indices.

4.1.2. PRISMA results

In addition to utilizing multispectral sensors such as L9 and S2, our study took a step forward by incorporating PRISMA hyperspectral data to enhance the distribution patterns of barite and iron ores within the study area. Employing various image-processing techniques allowed us to visualize and differentiate the exposed lithologies effectively. Notably, the first principal component of PRISMA data reasonably delineates the iron-bearing minerals and barite deposits with colour changes that coincided with our investigations (Fig. 10). These rocks appeared in distinctive red, while the surrounding yellow hues accurately represented the weathering products associated with them. Spectral analysis conducted in these areas unveiled a mixture of iron-



Fig. 12. Field photographs showing (a) a general view showing the intercalation between ferruginous and barite deposits; (b) barite concretions within bedding planes; (c) ferruginous ironstone; and (d) Banded Iron Formation (BIF).

bearing minerals and barite (Fig. 10a). To illustrate our findings, spectral profiles were generated along the VNIR-SWIR range for common iron minerals within the study area. These profiles were precisely resampled and compared with the areas of interest within the study area, as depicted in Figure 10b.

4.2. *Field observations*

Seventy vertical lithofacies sections around Wadi Halfa were carefully investigated to validate our findings. Four types of iron ore with more than three distinct layers were identified as shown in Fig. 11: (1) oolitic ironstone, (2) ferruginous sandstone, (3) ferruginous ironstone, and (4) Banded Iron Formation (BIF).

Three types of barite deposits were also found in the study area,

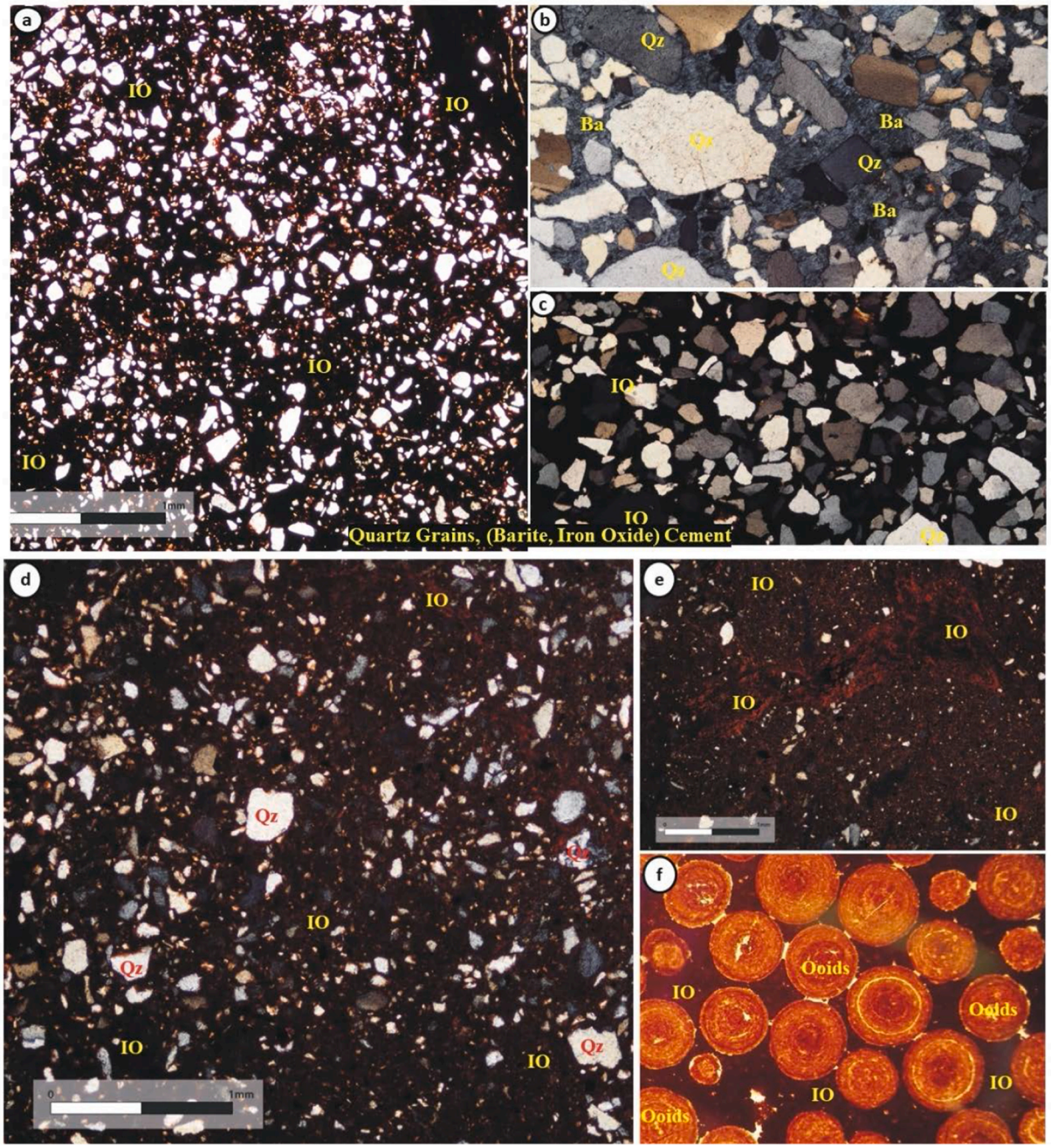


Fig. 13. (a) Photomicrograph showing the mineral composition of iron oxide (IO) between grains; (b) barite as cement in quartz grains; (c) the main cementing material is iron oxide, like hematite (opaques); (d) ferruginous ironstone; (e) hematite cement between grains of ferruginous sandstone; and (f) yellowish, brownish to dark brown oolitic ironstone.

corroding bedding planes of sandstone include: (1) barite concretions, (2) cementing material in sandstone, and (3) as fissure filling within bedding planes of Fig. 12.

4.3. Petrographical analyses

The oolitic ironstone represents the most common economic type of iron ore in the study area characterized by one to three layers with thicknesses ranging from 20 to 100 cm. The colours of oolitic ironstone vary from reddish to brownish, yellowish, and black. Under the microscope, oolites are moderate to well sorted, rounded to subrounded, and showing concentric layered ooid structure of yellowish, brownish to dark brown hematite as shown in Fig. 12. Most studied thin sections of other types of iron ore contain iron oxides with amounts ranging from 19 % to 49 %, averaging 34 % (Fig. 13a–d, and e). It is one of the principal cementing materials.

Barite occurs as concretions composed mainly of angular mono- and polycrystalline quartz grains (35.1–52.3 % and 2.0–20.9 %, respectively). Barite serves as the primary cementing material, ranging from 39.2 % to 44.1 %. Notably, some barite cement penetrates quartz grains, and crushing quartz grains have been observed (Fig. 13b).

Description of authigenic iron oxide and barite minerals under SEM is summarized in Fig. 14a, b, c, d, and e.

SEM-EDX provides elemental composition of minerals and cements, helping to identify their chemical origin. for instance, energy dispersive X-ray, the percentage of iron oxides ranges from 6 % to 14.7 % with an

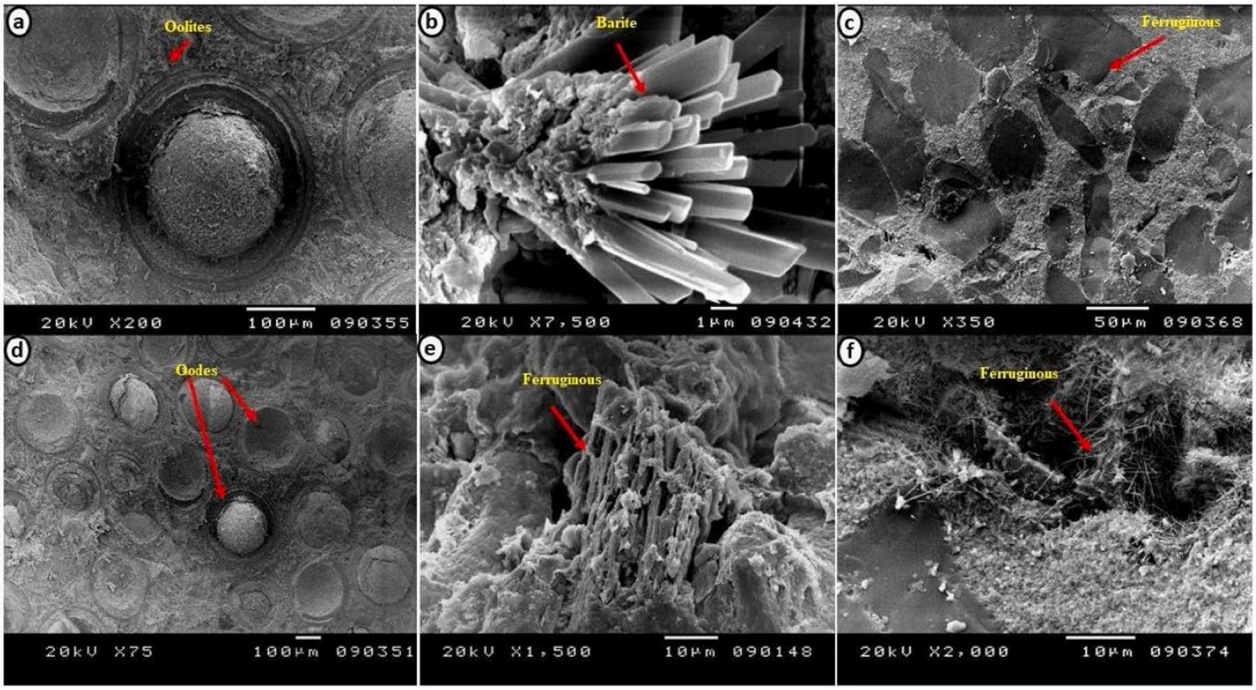


Fig. 14. SEM micrograph of (a) well-rounded concentric hematite-rich ooids alternating with hematite-rich sheaths in the inner core of ooids; (b) barium sulfate crystals; (c) hematite cement between grains of ferruginous sandstone; (d) the inner core of ooids; (e) hematite; and (f) perfect laths of elongate shape of hematite around authigenic quartz.

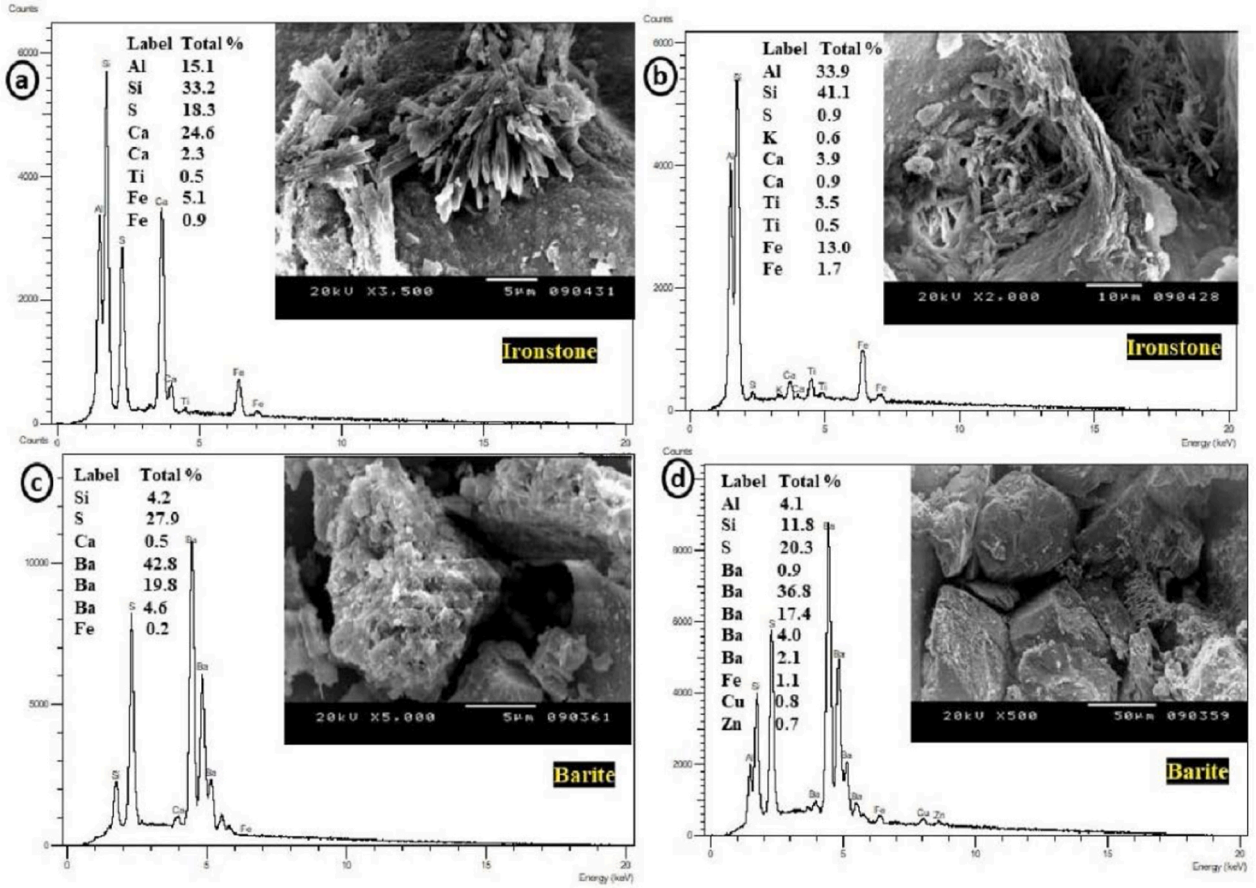


Fig. 15. (a) Ironstone under SEM EDX with high content of Ca; (b) Energy dispersive X-ray (EDX) of different ironstones; (c) EDX showing more than 50 % of barium sulfate; and (d) barite crystals under SEM with EDX of 54 % of barite.

Table 3
The average chemical composition of the oolitic ironstone samples from Wadi Halfa.

SiO_2	Al_2O_3	CaO	Cr_2O_3	Fe_2O_3	K_2O	MgO	MnO	Na_2O	P_2O_5	TiO_2	LOI (1000 °C)	Ba
10.84	4.0795	3.3759	0.0139	**62.72**	0.09	0.52	2.179	0.26	1.91	0.11	13.46	1164.39
Ce	**Dy**	**Er**	**Eu**	**Ga**	**Gd**	**Ho**	**La**	**Lu**	**Nb**	**Nd**	**Pr**	**Rb**
56.9043	8.6705	4.5110	2.2575	14.5404	9.1845	1.6649	20.4178	0.5674	3.8207	29.8910	7.1008	2.2201
Sc	**Sm**	**Sn**	**Sr**	**Tb**	**Th**	**Tm**	**U**	**V**	**W**	**Y**	**Yb**	**Zr**
5.2149	7.8415	2.9723	138.3714	1.4767	8.1575	0.6570	5.0896	615.08	10.36	45.8573	4.20095	41.2967

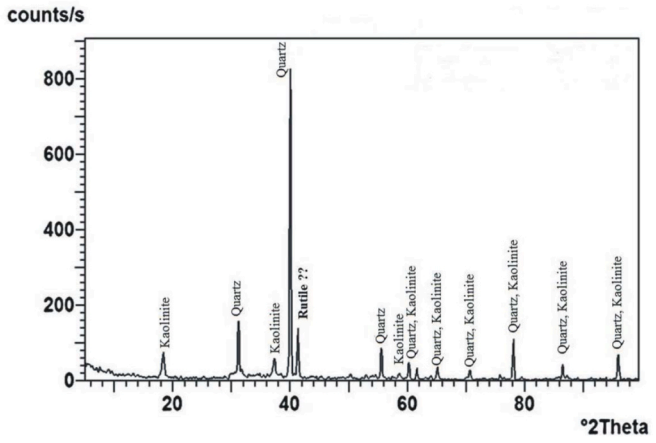


Fig. 16. X-ray powder diffraction showing that the predominant clay mineral is kaolinite.

average of 10.4 % as Fe (Fig. 15a and b), and for barite it ranges from 60.3 % to 67.4 % with an average of 63.9 % for Ba (Fig. 15c and d) which highly represents the concentration of barium in most studied samples.

The XRF results of oolitic ironstone type represent the main iron ore in the selected areas, which estimated appropriate amounts of total iron oxides (62.7 %), and other trace elements such as SiO_2 (10.84 %), Al_2O_3 (4.08 %), Na_2O (0.26 %), and P_2O_5 (1.91 %) as summarized in Table 3.

The X-ray powder diffraction results reveal that the predominant clay mineral identified in all studied samples is kaolinite, which is consistent as the primary type of clay mineral. These findings align with similar results obtained from the detection of hydroxyl-bearing minerals using L9 and S2 data, as illustrated in (Figs. 4c and 7a). The spatial and spectral patterns observed in L9 and S2 imagery support the presence of kaolinite, providing complementary evidence for the mineralogical composition of the samples studied (Fig. 16).

4.4. Machine learning classification and anomaly outcomes

The supervised machine learning-based classification of lithological units and mineralized zones of WHOI generated high-accuracy maps and results (Fig. 17a and Table 3), effectively distinguishing Permo-Triassic iron ore and barite deposits, and the surrounding Cretaceous sandstone sedimentary sequences. The integration of multispectral (L9, L8, aS2) and hyperspectral (PRISMA) data (Fig. 9), along with band ratios for ferric, ferrous, hydroxyl, and barite minerals, significantly enhanced mineral detection. The classified lithological map of algorithms (MLW, SVM, MDC) (Fig. 17b, c, and d, respectively) reveals distinct zones of ironstone (iron ore), barite deposits, surrounding Cretaceous sandstone, and Quaternary and recent sediments, aligning with field observations. The detected iron-rich anomalies are primarily concentrated in WHOI.

A confusion matrix summarizing classification accuracy is presented in Table 4, showing minimal misclassification errors across different lithological units.

The accuracy of the four classifier algorithms (ANN, SVM, MDC, MLC) shows that Lake Nubia has an accuracy of 100 % due to its impurity compared to other lithological units. For the ANN algorithms, ironstone was correctly classified with an accuracy of 100 % and an average of 83 % for the sandstone and Quaternary deposits (Fig. 17).

The classification results indicate that the MDC achieved the highest overall accuracy (98.99 %) with minimal commission and omission errors, making it the most reliable classifier (Fig. 17a). ANN also performed well, demonstrating high classification accuracy with slightly lower performance compared to SVM (Fig. 17c). MLC showed strong results (97.45 %) but exhibited a higher omission error for Quaternary deposits (10.21 %), this is due to interconnection between the weathered sandstone and the recent deposits which have similar mineral composition, making their distinction more complex (Fig. 17b). Meanwhile, the ANN had an overall accuracy of 94.59 %, and showed a significant omission error for Quaternary deposits of 22.55 %, indicating misclassification issues in this unit similarly to MLC (Fig. 17d). The confusion matrix confirms that ANN and SVM performed better in correctly classifying sedimentary sequences, whereas MDC struggled with ironstone and sandstone classification. Overall, ANN and SVM remain the most effective approaches, with MLC and MDC performing slightly less effectively.

The final lithological map of the Wadi Halfa area was generated using the ANN classifier, which demonstrated improved accuracy in distinguishing lithological units and delineating iron ore occurrences (Fig. 18).

5. Discussion

The integration of Landsat 9, 8 (L9 & 8) and Sentinel-2 (S2) imagery for lithological mapping of sedimentary rocks has demonstrated significant effectiveness, particularly in delineating sedimentary facies changes related to their depositional environments and age (Askari et al., 2018; Kabolizadeh et al., 2022). This integration was validated through detailed fieldwork and petrographic analyses of various rock units. The results indicated that the combined use of L8 and S2 imagery outperformed other combinations, providing superior insights into the geological variations spanning the Precambrian, Permo-Triassic, and Lower Jurassic to Cretaceous periods.

The results of the current study have important implications for mineral exploration and lithological mapping in similar sedimentary sequences within arid regions across Northeast Africa and globally. By representing the effective integration of multi-sensor remote sensing data (L9, L8, S2, and PRISMA) with advanced machine learning algorithms (ANN and SVM), supported by detailed field observations and laboratory analyses, this study offers a scalable, cost-effective workflow (see Figs. 12, 14 and 17). It can be applied in geologically comparable terrains to enhance the detection of industrial minerals such as iron ore and barite, particularly in underexplored or inaccessible areas.

The high classification accuracy achieved is attributed to the distinct spectral signatures of these minerals and the relatively simple lithological context of the study area dominated by ironstone, sandstone, Quaternary deposits, and a well-defined water body making it a valuable model for comparable terrains.

Specifically, band combinations such as (R6/7-G4/3-G4/6) and (R6/7-5/4-G6/7-B5/6) in L8 and L9, respectively, alongside (R11/12-G4/2-B4/11) by S2, were particularly effective in highlighting significant geological variations. These combinations successfully distinguished the Precambrian basement complex from the Permo-Triassic sandstone,

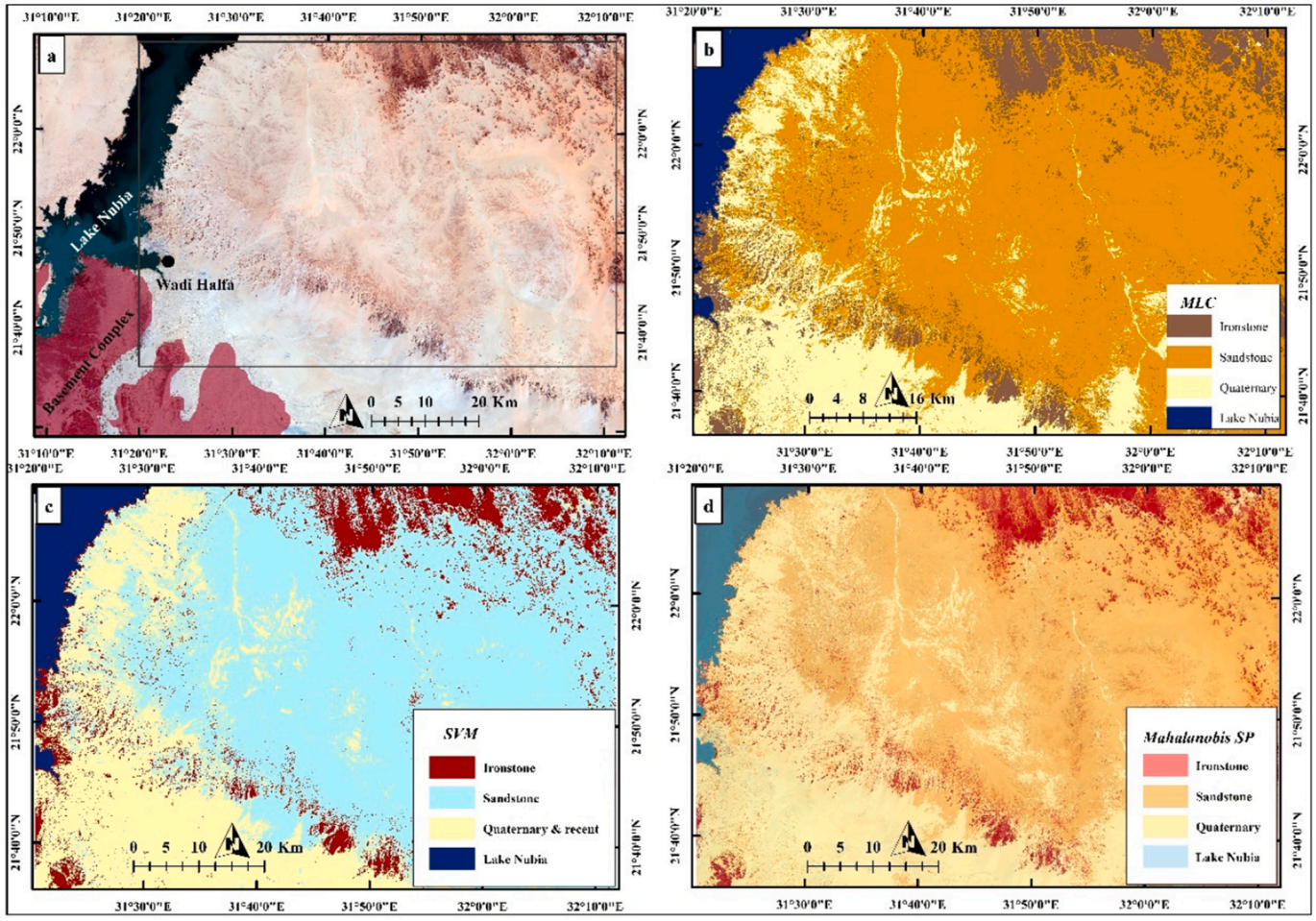


Fig. 17. (a) L9 RGB map showing the selected area for classification; (b) MLW classified map; (c) SVM map; (d) MDC lithological map of the study area.

Table 4
Overall accuracy and class-level metrics.

Classifier	Overall Accuracy %	Kappa	Ironstone Prod. Acc. (%)	Ironstone User Acc. (%)	Sandstone Prod. Acc. (%)	Sandstone User Acc. (%)	Quaternary Prod. Acc. (%)	Quaternary User Acc. (%)	Lake Nubia Prod. Acc. (%)	Lake Nubia User Acc. (%)
ANN	94.59	0.928	100	100	100	82.85	77.45	100	100	100
SVM	95.51	0.940	100	100	100	85.33	81.28	100	100	100
MLC	97.45	0.966	100	99.59	100	91.43	89.79	100	99.59	100
MDC	98.99	0.986	99.18	100	96.88	99.20	100	96.71	100	100

including various layers of oolitic ironstone, and Lower Jurassic to Cretaceous sandstone, which encompasses significant deposits of iron ore and barite. These findings are corroborated by studies conducted in the El Bir area, Southern North Sudan, which identified significant titano-magnetite deposits within the basement complex (Nafi et al., 2015). Similarly, spectral profiles indicating ferric oxide absorption features, such as (4/3) and (12/8A + 3/4), align with observations made in Cuprite, Nevada (Ge et al., 2020).

The spectral profiles obtained from the study areas demonstrated a notable similarity to the combined signatures of barite, hematite, and goethite. Validation of these spectral signatures was achieved through on-site field observations, petrographic examinations, X-ray diffraction (XRD) analysis, and scanning electron microscopy (SEM) imaging. The convergence of findings from these diverse methodologies confirmed the actual distribution patterns of iron-bearing minerals and barite in the studied terrain.

When compared with data from L9, L8, S2, and PRISMA maps, areas with high iron and barium content were consistently highlighted, represented by high-density colour slices. This comparative analysis revealed two regions with significant concentrations of iron ore and barite standing out against other locations. Representative samples from these regions showed a high quality of oolitic ironstone and barite, with a high content of iron oxide and barium sulfate, which can be efficiently separated from other elements, making them highly suitable for the steel industry and shielding concrete, respectively.

The performance of different advanced machine learning algorithms, including ANN, SVM, MDC, and MLC, was evaluated to determine their effectiveness in lithological mapping and mineralized zone detection. Among these, MDC demonstrated the highest overall accuracy (98.99 %) with minimal commission and omission errors, making it the most reliable model for distinguishing different lithological units within the study area. This is particularly significant for complex sedimentary sequences, where machine learning applications remain relatively uncommon and less well-defined in previous studies (Mohamed et al.,

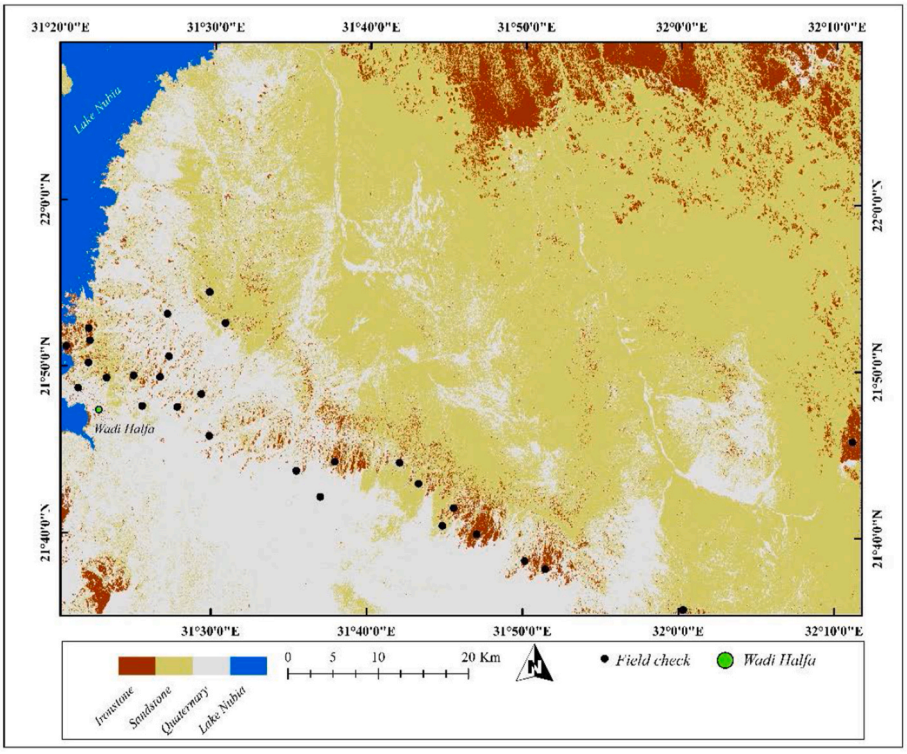


Fig. 18. Final geological map of the study area generated by Artificial Neural Network.

2019; Tsangaratos et al., 2025; Verbovšek and Popit, 2018).

The high accuracy of the ANN model in the current study can be attributed to several key factors compared to recent previous studies (Ayoobi and Tangestani, 2017; Chen et al., 2023; Elahi et al., 2022; Shebl et al., 2022; Shebl and Csámer, 2021; Shirmard et al., 2022). One primary reason is the limited number of lithological units within the study area, consisting of only three distinct rock types (ironstone, sandstone, and Quaternary deposits). Additionally, the presence of Lake Nubia, a well-defined water body, supported the model's performance, as water bodies are easily distinguishable due to their single spectral characteristics.

SVM also performed well, providing competitive accuracy while effectively handling non-linear relationships within the dataset. In contrast, the MLC, although achieving relatively high accuracy (97.45 %), exhibited higher omission errors, particularly in the ironstone class, due to spectral overlap with other lithological units. This suggests that while Mahalanobis is efficient for relatively homogeneous classes, it struggles in areas with significant spectral mixing. Overall, ANN and SVM developed as the most robust classifier for this study, while MDC proved useful for describing complex spectral variations, and MLC remained a sustainable option for less complex terrains.

The vertical lithofacies of the ironstone sections typically begin with medium to coarse-grained, yellowish to brownish trough cross-bedded ferruginous sandstone, planar cross-bedded sandstone facies. The upper sections consist of fine to medium-grained ferruginous sandstone interspersed with siltstone. This unit is intercalated with three distinct layers of oolitic ironstone varying in thickness and color.

The barite deposit sections exhibit vertical lithofacies starting with medium-grained yellowish sandstone cemented predominantly by barite, overlain by coarse-grained trough cross-bedded sandstone. The lower fining upward sequence transitions to a poorly sorted yellowish coarse-grained sandstone containing barite concretions of various sizes and shapes. These concretions penetrate the bedding planes of sandstone. The upper sections comprise fine to medium-grained yellowish sandstone facies cemented by barite, transitioning to ferruginous sandstone, and capped by fine to medium-grey siltstone facies. Additionally, substantial wadi deposits composed mainly of sand, silt, and barite gravel were observed between these sections.

Four types of iron ore with more than three distinct layers were identified, including: oolitic ironstone; ferruginous sandstone; ferruginous ironstone; and banded ironstone formation.

Field observations of potential iron ore and barite deposits were consistent with findings derived from L8, L9, S2, and PRISMA imagery, followed by machine learning algorithms (Figs. 17 and 18). The multi-scale map of Wadi Halfa, illustrated in Figure (19), aligns closely with these observations, confirming the presence of iron ore and barite deposits. This comprehensive approach underscores the effectiveness of integrating remote sensing data with ground-truth validation to enhance the accuracy and reliability of lithological mapping in sedimentary terrains.

The iron ores found in Wadi Halfa, characterized by ferruginous sandstone and oolitic ironstone, display a distribution of colours ranging from reddish, brownish, yellowish, and purple to black. These oolites, visible to the naked eye, typically measure less than 2 mm in diameter. Some oolites in Wadi Halfa exhibit pipes and concretions.

Thin sections of different iron ores commonly reveal iron oxides as the predominant cementing material, suggesting a high-oxidation environment. This observation points to the presence of shallow marine oolitic ironstone formations in North Sudan and South Egypt.

Barite concretions recorded in the different parts of the study area penetrate the sandstone layers parallel to bedding planes as concretions of composite grains, such as those with a discoidal shape, which also occur as cement.

The chemical analysis of oolitic ironstone type represents the main iron ore in the selected areas, which estimated iron oxides and other associated elements, whereas chemically under energy dispersive X-ray (EDX), showing highly represents of barium (63.9 %) in most studied samples.

These results of representative samples indicate the good quality of the oolitic ironstone in the study area. The average iron oxide content reaches 62.7 %, and it can be easily separated from other chemical components.

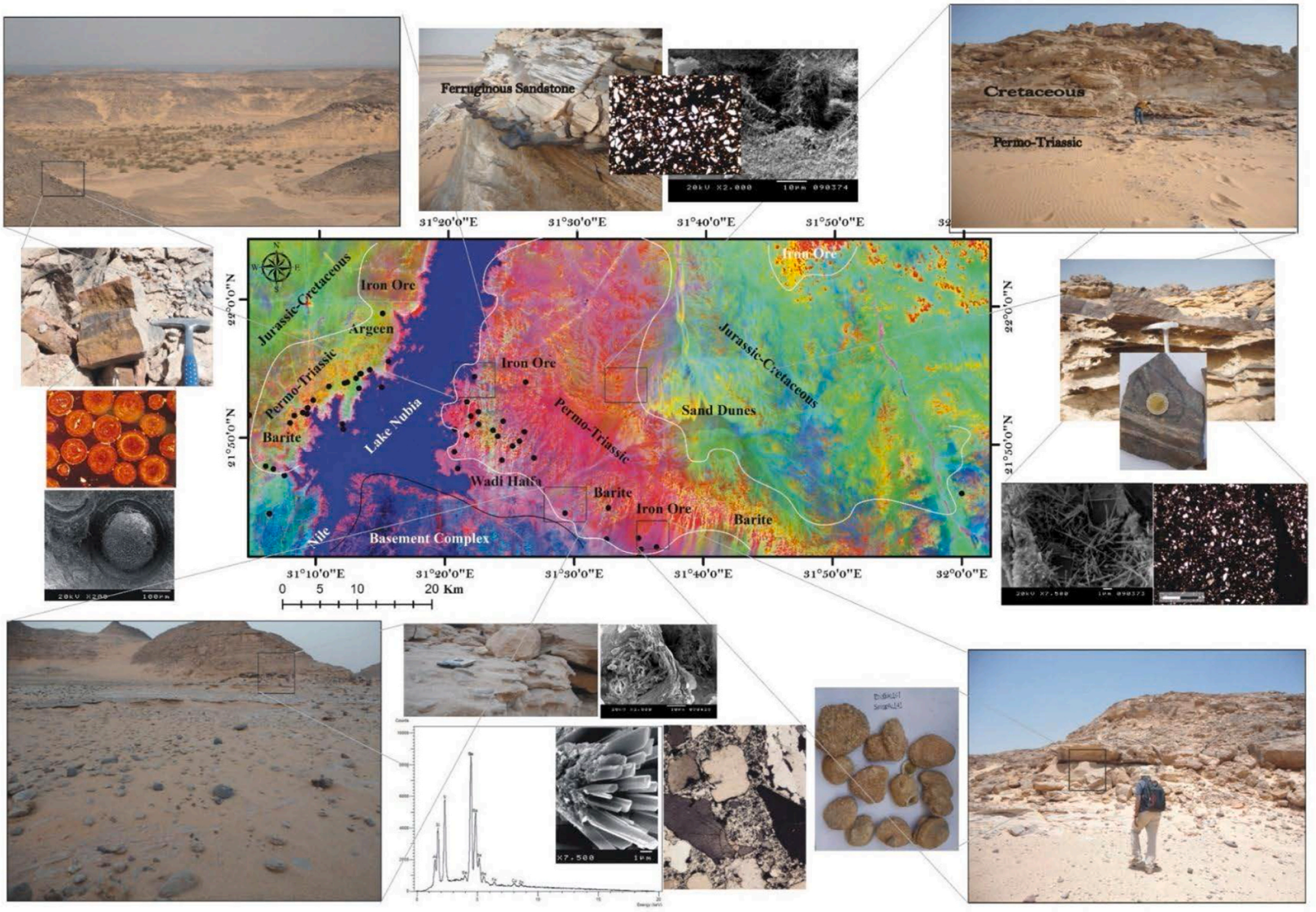


Fig. 19. Multiscale detection of iron ore and barite deposits verified by field observations and laboratory study.

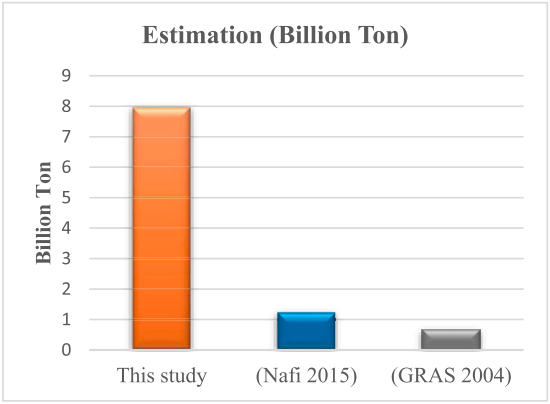


Fig. 20. Geological reserve estimation in the current research compared to those of previous studies.

Utilizing data from mega-scale satellite images (L9, S2, and PRISMA) and progressing from broad field macro-observations to detailed micro-analyses in the laboratory (utilizing techniques like polarizing microscopy, SEM-EDX, XRD, and XRF), our investigation estimates a potential total iron ore reserve exceeding 7.963×10^9 tons based on the simple geological equation for ore reserve (1) using parameters (area: 3570.77 km^2; thickness: 20–100 cm; and density 2.23 g/cm^2) for oolitic iron ore compared to a recent study conducted by Nafi et al. (2015), which reported a total of 1.234×10^9 tons with an average concentration of Fe_2O_3 (41.29), our findings highlight to reassess current iron ore occurrences using an integration of multispectral and hyperspectral remote sensing, considering the updated and more accurate estimates and can help us to understand long-term planning for sustainable extraction for iron ore. Conversely, the evaluation of barite reserves demands more comprehensive fieldwork to ensure accurate resource estimation.

$$ore\ reserve = area \times thickness \times density \quad (1)$$

The volume (V) was calculated for both minimum and maximum thicknesses of 20 cm (7.14154×10^{14} cm^3) and 80 cm (2.856616×10^{15} cm^3), respectively.

The mass (M) of the ore was then determined by multiplying the volume by the density (1.5925782×10^9 and 6.370312×10^9 metric tons) for minimum and maximum thickness, respectively.

The calculated total ore reserve, depending on the thickness of the ore body (20–80 cm), is almost 8 billion (7.9628902×10^9) tons. These estimates provide a substantial basis for further exploration and potential extraction planning (Fig. 20).

6. Conclusions

The present study successfully integrated multi-sensor remote sensing data (Landsat 9 & 8, Sentinel-2, and PRISMA) with field observations and laboratory analyses to identify and evaluate iron ore and barite deposits in the Wadi Halfa area, Northern Sudan. Key spectral indices and band ratios were used to detect and delineate mineralized zones, with the FCC combinations of L9 (R6-G3-B1) and S2 (R5-G2-B1) as an optimum index factor proving especially effective in highlighting geological variations across the region.

The machine learning-based lithological map revealed distinct rock units, including Precambrian basement rocks and sedimentary sequences from the Permo-Triassic to Lower Cretaceous. Validation through petrographic, XRD, XRF, and SEM analyses confirmed the presence and distribution of iron ore and barite-rich units.

Four major iron ore types were identified: oolitic ironstone, ferruginous sandstone, ferruginous ironstone, and banded iron formation alongside barite concretions. The integration of spectral analysis and field data led to an estimated reserve of over 7.9 billion tons of iron ore with an average Fe_2O_3 content of 61 %, significantly exceeding previous assessments.

Moreover, advanced machine learning algorithms (ANN and SVM) outperformed traditional methods in lithological classification, benefitting from the relatively simple spectral signatures of the minerals and the limited number of lithological classes. These findings underline the need for further research into AI-driven exploration techniques to optimize the identification and lithological mapping of critical mineral resources in similar terrains.

7. Limitations and recommendations for future work

Throughout this study, investigates an extensive dataset combining multi-sensor remote sensing, detailed field observations and petrographic, XRD, XRF, and SEM analyses, various aspects necessitate deeper investigation. In particular, a more targeted geochemical analysis is recommended to explain the distribution and origin of the oolitic ironstone and the barite within sediments, especially in determining whether their formation is linked to biogenic or abiogenic processes, as well as assessing possible hydrothermal activities or other mineralizing mechanisms.

Although the current field observations covered key exposures across the Wadi Halfa area, future work should extend to producing continuous stratigraphic columns of the region, particularly the distribution of iron ore and barite-bearing sediments, supported by borehole data and subsurface profiling, to refine the stratigraphic column of the Nubian Sandstone Formation, focusing on the Wadi Halfa Oolitic Ironstone (WHOI).

Following the determination of the origin of barite in sandstone, detailed mineralogical studies should be carried out to map the distribution of clay minerals, particularly kaolinite, illite, and other phyllosilicates, which may hold a significant impact for diagenetic history and resource potential. An equally important priority is the reconstruction of the depositional environment of the WHOI through advanced geochemical and isotopic analyses, which could provide detailed paleoenvironmental conditions and mineralization processes.

The application of hyperspectral remote sensing could also be expanded to detect and map a wider range of metallic and non-metallic minerals and potentially hazardous materials, such as uranium-bearing sandstones. Processing higher spectral-resolution datasets could considerably improve mineral discrimination and aid in environmental assessments.

Finally, while the machine learning approaches (ANN and SVM) achieved high accuracy and anomaly detections due to the clear spectral signatures and limited number of lithological units, performance could be further improved through the integration of larger, more varied training datasets, deep learning, and additional geochemical and mineralogical parameters. Such improvements would enhance AI-driven exploration workflows in similar geological settings.

CRediT authorship contribution statement

Abazar M.A. Daoud: Writing – original draft, Validation, Software, Methodology, Investigation, Formal analysis, Data curation, Conceptualization. **Ali Shebl:** Validation, Software, Methodology, Formal analysis, Data curation, Conceptualization. **Mutwakil Nafi:** Visualization, Validation, Methodology, Data curation, Conceptualization. **Abdelmajeed A. Elrasheed:** Software, Methodology, Formal analysis. **Árpád Csámer:** Writing – review & editing, Visualization, Conceptualization. **Péter Rózsa:** Writing – review & editing, Visualization, Validation, Supervision, Resources, Project administration, Conceptualization.

Declaration of competing interest

The authors declare that they have no known competing financial

interests or personal relationships that could have appeared to influence the work reported in this article.

I the undersigned declared that this manuscript is original, has not been published before and is not currently being considered for publication elsewhere.

We confirm that the manuscript has been read and approved by all named authors and that there are no other persons who satisfied the criteria for authorship but are not listed. We further confirm that the order of authors listed in the manuscript has been approved by all of us.

All the authors understand that the Corresponding Author is the sole contact for the Editorial process. He is responsible for communicating with the other authors about progress, submissions of revisions and final approval of proofs.

Acknowledgment

The authors would like to express their sincere gratitude to Dr. Richard William McIntosh for the thorough English language review and valuable linguistic improvements to the manuscript. Special thanks are also extended to the Stipendium Hungaricum Scholarship Program for their generous support. This work is part of a joint academic collaboration between Hungary and Sudan under the framework of the Stipendium Hungaricum Scholarship, through which Abazar is currently pursuing his studies.

Data availability

Data will be made available on request.

References

Abay, H.H., Legesse, D., Venkata Suryabhagavan, K., Atnafu, B., 2022. Mapping of ferric (Fe3+) and ferrous (Fe2+) iron oxides distribution using ASTER and landsat 8 OLI data, in Negash Lateritic iron deposit, Northern Ethiopia. Geology, Ecology, and Landscapes. https://doi.org/10.1080/24749508.2022.2130556.

Abdelkareem, M., Al-Arifi, N., 2021. Synergy of remote sensing data for exploring hydrothermal mineral resources using GIS-based fuzzy logic approach. Remote Sens. 13 (22). https://doi.org/10.3390/rs13224492.

Abdelrahman, S., Ibrahim, M.A.E., Li, H., Abdel Rahman, E.M., Faisal, M., 2024. Geochemical characteristics of Neoproterozoic metavolcanic rocks of Ariab Auriferous Volcanogenic Massive Sulfide deposit, Red Sea hills, North-East Sudan. J. Afr. Earth Sci. 216, 105305. https://doi.org/10.1016/j.jafrearsci.2024.105305.

Abdelsalam, M.G., Liégeois, J.-P., Stern, R.J., 2002. The Saharan metacraton. J. Afr. Earth Sci. 34 (3–4), 119–136. https://doi.org/10.1016/S0899-5362(02)00013-1.

Abu-Fatima, M., Marignac, C., Cathelineau, M., Boiron, M.C., 2021. Metallogeny of a Pan-African oceanic arc: VHMS and gold deposits in the Ariab-Arbaat belt, Haya terrane, Red Sea Hills (Sudan). Gondwana Res. 98, 76–106. https://doi.org/10.1016/j.gr.2021.06.001.

Askari, G., Pour, A.B., Pradhan, B., Sarfi, M., Nazemnejad, F., 2018. Band ratios matrix transformation (BRMT): a sedimentary lithology mapping approach using ASTER satellite sensor. Sensors 18 (10). https://doi.org/10.3390/s18103213.

Ayoobi, I., Tangestani, M.H., 2017. The effect of minimum noise fraction data input on success of artificial neural network in lithological mapping of a magmatic terrain with ASTER data; A case study from SE Iran. Remote Sens. Appl.: Society and Environment 7, 21–26. https://doi.org/10.1016/j.rsase.2017.06.001.

Bedini, E., 2017. The use of hyperspectral remote sensing for mineral exploration: a review. Journal of Hyperspectral Remote Sensing 7 (4), 189–211. https://doi.org/10.29150/jhrs.v7.4.p189-211.

Chen, Y., Dong, Y., Wang, Y., Zhang, F., Liu, G., Sun, P., 2023. Machine learning algorithms for lithological mapping using Sentinel-2 and SRTM DEM in highly vegetated areas. Frontiers in Ecology and Evolution 11. https://doi.org/10.3389/fevo.2023.1250971.

Costa, I.S.L., Serafim, I.c. c. de O., Tavares, F.M., Polo, h. j. de O., 2020. Uranium anomalies detection through Random Forest regression. Explor. Geophys. 51 (5), 555–569. https://doi.org/10.1080/08123985.2020.1725387.

Daoud, A.M.A., Rashed, M.A., Sediek, K.N., Elamein, A.M., Elsharief, A.M., 2020. Barite concretions in wadi Halfa oolitic ironstone Formation, north Sudan. Journal of Geography, Environment and Earth Science International 51–64. https://doi.org/10.9734/jgeesi/2020/v24i530227.

Daoud, A.M.A., Rashed, M.A., Sediek, K.N., Elsharief, A.M., Elamein, A.M., 2021. Petrography, diagenesis and paragenesis of wadi Halfa oolitic ironstone Formation, north Sudan. Eur. J. Appl. Sci. 9 (3). https://doi.org/10.14738/aivp.93.10461.

Daoud, A.M.A., Abdelkader, M.M., Sediek, K.N., Elsharief, A.M., Rashed, M.A., Elamein, A.M., Abdalrahiem, K.O., Rózsa, P., 2024. Relationship between petrography and geomechanical properties of the sandstone: a case study from Wadi Halfa, North Sudan. International Review of Applied Sciences and Engineering. https://doi.org/10.1556/1848.2024.00883.

Daoud, A.M.A., Shebl, A., Abdelkader, M.M., Mohieldain, A.A., Csámer, Á., Satti, A.M.N., Rózsa, P., 2025. Remote sensing and gravity investigations for barite detection in Neoproterozoic rocks in the Ariab area, Red Sea Hills, Sudan. Remote Sens. Appl.: Society and Environment 37. https://doi.org/10.1016/j.rsase.2024.101416.

Doner, N., Pargan, A.R., Aygahoglu, A., Liu, F., Sen, F., 2019. Radiative properties of hematite particles in the UV-visible spectrum. Int. J. Therm. Sci. 139, 79–87. https://doi.org/10.1016/j.ijthermalsci.2019.02.006.

Elahi, F., Muhammad, K., Din, S.U., Khan, M.F.A., Bashir, S., Hanif, M., 2022. Lithological mapping of Kohat Basin in Pakistan using multispectral remote sensing data: a comparison of Support Vector Machine (SVM) and Artificial Neural Network (ANN). Appl. Sci. 12 (23), 12147. https://doi.org/10.3390/app122312147.

Eldosouky, A.M., El-Qassas, R.A.Y., Pour, A.B., Mohamed, H., Sekandari, M., 2021. Integration of ASTER satellite imagery and 3D inversion of aeromagnetic data for deep mineral exploration. Adv. Space Res. 68 (9), 3641–3662. https://doi.org/10.1016/j.asr.2021.07.016.

El-Omairi, M.A., El Garouani, M., El Garouani, A., 2025. Enhanced lithological mapping via remote sensing: employing SVM, random trees, ANN, with MNF and PCA transformations. The Egyptian Journal of Remote Sensing and Space Sciences 28 (1), 34–52. https://doi.org/10.1016/j.ejrs.2024.12.001.

Elsayed Zeinelabdein, K.A., El-Nadi, A.H.H., Babiker, I.S., 2020. Prospecting for gold mineralization with the use of remote sensing and GIS technology in North Kordofan State, central Sudan. Sci. Afr. 10. https://doi.org/10.1016/j.sciaf.2020.e00627.

Elsheikh, A., Zeinelabdein, K.A.E., Hag, S.O., Khidir, E., Elsheikh, A.E.M., El-Khidir, S.O. H., 2014. The use of remote sensing and GIS techniques as a guide to other geological methods for groundwater investigations in Hamisana Basement terrains, Red Sea hills, NE Sudan. International Journal of Geosciences and Geomatics 2 (2). https://www.researchgate.net/publication/268391718.

Evans, D., 1988. Multisensor classification of sedimentary rocks. Rem. Sens. Environ. 25 (2), 129–144. https://doi.org/10.1016/0034-4257(88)90097-1.

Ge, W., Cheng, Q., Jing, L., Wang, F., Zhao, M., Ding, H., 2020. Assessment of the capability of sentinel-2 imagery for iron-bearing minerals mapping: a case study in the cuprite area, nevada. Remote Sens. 12 (18). https://doi.org/10.3390/RS12183028.

Hayes, S.M., McCullough, E.A., 2018. Critical minerals: a review of elemental trends in comprehensive criticality studies. Resour. Policy 59, 192–199. https://doi.org/10.1016/j.resourpol.2018.06.015.

Jain, R., 2021. Feature-Oriented Principal Component Selection (FPCS) for delineation of the geological units using the integration of SWIR and TIR ASTER data. In: Marghany, M. (Ed.), Recent Remote Sensing Sensor Applications. IntechOpen. https://doi.org/10.5772/intechopen.99046. Ch. 6).

Kabolizadeh, M., Rangzan, K., Mousavi, S.S., Azhdari, E., 2022. Applying optimum fusion method to improve lithological mapping of sedimentary rocks using sentinel-2 and ASTER satellite images. Earth Science Informatics 15 (3), 1765–1778. https://doi.org/10.1007/s12145-022-00836-1.

Lemdjou, Y.B., Tchato Tchaptchet, D.P.I., Li, H., Whattam, S.A., Soh Tamehe, L., Elatikpo, S.M., Madayipu, N., 2022. Cambrian mafic magmatism in the Kékem area, NW edge of the Adamawa-Yadé domain, Central African Fold Belt: implications for Western Gondwana dynamics. Precambr. Res. 380, 106840. https://doi.org/10.1016/j.precamres.2022.106840.

Li, F., Zhang, P., Ma, X., Yuan, G., 2021. The iron oolitic deposits of the lower Devonian Yangmaba formation in the Longmenshan area, Sichuan Basin. Mar. Petrol. Geol. 130. https://doi.org/10.1016/j.marpetgeo.2021.105137.

Mahboob, M.A., Celik, T., Genc, B., 2024. Predictive modelling of mineral prospectivity using satellite remote sensing and machine learning algorithms. Remote Sens. Appl.: Society and Environment 36, 101316. https://doi.org/10.1016/j.rsase.2024.101316.

Mohamed, I.M., Mohamed, S., Mazher, I., Chester, P., 2019. Formation lithology classification: insights into machine learning methods. In: SPE Annual Technical Conference and Exhibition. https://doi.org/10.2118/196096-MS.

Mohamed Taha, A.M., Xi, Y., He, Q., Hu, A., Wang, S., Liu, X., 2023. Investigating the capabilities of various multispectral remote sensors data to map mineral prospectivity based on random Forest predictive model: a case Study for gold deposits in Hamissana Area, NE Sudan. Minerals 13 (1). https://doi.org/10.3390/min13010049.

Nafi, M., Amein, A. El, Dawi, M. El, Salih, K., 2015. Wadi Halfa oolitic ironstone Formation, wadi Halfa and argein areas, north Sudan. World Academy of Science, Engineering and Technology, Open Science Index 106. Int. J. Environ. Ecol. Eng. 9 (10), 1290–1295. https://doi.org/10.5281/zenodo.1109924.

Ninomiya, Y., Fu, B., 2019. Thermal infrared multispectral remote sensing of lithology and mineralogy based on spectral properties of materials. Ore Geol. Rev. 108, 54–72. https://doi.org/10.1016/j.oregeorev.2018.03.012. Elsevier B.V.

Noda, S., Yamaguchi, Y., 2017. Estimation of surface iron oxide abundance with suppression of grain size and topography effects. Ore Geol. Rev. 83, 312–320. https://doi.org/10.1016/j.oregeorev.2016.12.019.

Nwaila, G.T., Zhang, S.E., Bourdeau, J.E., Ghorbani, Y., Carranza, E.J.M., 2022. Artificial intelligence-based anomaly detection of the Assen iron deposit in South Africa using remote sensing data from the Landsat-8 Operational Land Imager. Artificial Intelligence in Geosciences 3, 71–85. https://doi.org/10.1016/j.aiig.2022.10.001.

Penaloza, I., Tita, A., McNew, E., Chu, P., 2023. Barite resources, production and recovery using froth flotation: a review. Miner. Eng. 203, 108327. https://doi.org/10.1016/j.mineng.2023.108327.

Petropoulos, G.P., Kalaitzidis, C., Prasad Vadrevu, K., 2012. Support vector machines and object-based classification for obtaining land-use/cover cartography from Hyperion hyperspectral imagery. Comput. Geosci. 41, 99–107. https://doi.org/10.1016/j.cageo.2011.08.019.

Pour, A.B., Park, T.Y.S., Park, Y., Hong, J.K., Muslim, A.M., Läufer, A., Crispini, L., Pradhan, B., Zoheir, B., Rahmani, O., Hashim, M., Hossain, M.S., 2019. Landsat-8, advanced spaceborne thermal emission and reflection radiometer, and WorldView-3 multispectral satellite imagery for prospecting copper-gold mineralization in the northeastern Inglefield Mobile Belt (IMB), northwest Greenland. Remote Sens. 11 (20). https://doi.org/10.3390/rs11202430.

Rajan Girija, R., Mayappan, S., 2019. Mapping of mineral resources and lithological units: a review of remote sensing techniques. International Journal of Image and Data Fusion 10 (2), 79–106. https://doi.org/10.1080/19479832.2019.1589585.

Rockwell, B.W., Gnesda, W.R., Hofstra, A.H., 2021. Improved Automated Identification and Mapping of Iron Sulfate Minerals, Other Mineral Groups, and Vegetation using Landsat 8 Operational Land Imager Data, San Juan Mountains, Colorado, and Four Corners Region (No. 3466). US Geological Survey. https://doi.org/10.3133/sim3466.

Salem, S.M., El Gammal, E.A., 2015. Iron ore prospection East Aswan, Egypt, using remote sensing techniques. Egyptian Journal of Remote Sensing and Space Science 18 (2), 195–206. https://doi.org/10.1016/j.ejrs.2015.04.003.

Sankhya, A., 2018. Reprint of: mahalanobis, P.C. (1936) "On the Generalised Distance in Statistics.". The Indian Journal of Statistics 80 (S1), 1–7. https://doi.org/10.1007/s13171-019-00164-5.

Schandelmeier, H., Richter, A., Harms, U., 1987. Proterozoic deformation of the east Saharan craton in Southeast Libya, south Egypt and north Sudan. Tectonophysics 140 (2–4), 233–246. https://doi.org/10.1016/0040-1951(87)90231-9.

Shebl, A., Abriha, D., Dawoud, M., Ali Hussein Ali, M., Csámer, Á., 2024. PRISMA vs. Landsat 9 in lithological mapping – a K-fold Cross-Validation implementation with Random Forest. Egyptian Journal of Remote Sensing and Space Science 27 (3), 577–596. https://doi.org/10.1016/j.ejrs.2024.07.003.

Shebl, A., Csámer, Á., 2021. Stacked vector multi-source lithologic classification utilizing Machine Learning Algorithms: data potentiality and dimensionality monitoring. Remote Sens. Appl.: Society and Environment 24, 100643. https://doi.org/10.1016/j.rsase.2021.100643.

Shebl, A., Hamdy, M., 2023. Multiscale (microscopic to remote sensing) preliminary exploration of auriferous-uraniferous marbles: a case study from the Egyptian Nubian Shield. Sci. Rep. 13 (1). https://doi.org/10.1038/s41598-023-36388-7.

Shebl, A., Kusky, T., Csámer, Á., 2022. Advanced land imager superiority in lithological classification utilizing machine learning algorithms. Arabian J. Geosci. 15 (9), 923. https://doi.org/10.1007/s12517-022-09948-w.

Shirmard, H., Farahbakhsh, E., Heidari, E., Beiranvand Pour, A., Pradhan, B., Müller, D., Chandra, R., 2022a. A comparative Study of convolutional neural networks and conventional machine learning models for lithological mapping using remote sensing data. Remote Sens. 14 (4), 819. https://doi.org/10.3390/rs14040819.

Shirmard, H., Farahbakhsh, E., Müller, R.D., Chandra, R., 2022b. A review of machine learning in processing remote sensing data for mineral exploration. Rem. Sens. Environ. 268, 112750. https://doi.org/10.1016/j.rse.2021.112750.

Stern, R.J., Kroner, A., Bender, R., Reischmann, T., Dawoud, A.S., 1994. Precambrian basement around Wadi Halfa, Sudan: a new perspective on the evolution of the East Saharan Craton. Geol. Rundsch. 83 (3), 564–577. https://doi.org/10.1007/bf01083228.

Su, Q., Yu, H., Xu, X., Chen, B., Yang, L., Fu, T., Liu, W., Chen, G., 2023. Using Principal Component Analysis (PCA) combined with multivariate change-point analysis to identify brine layers based on the geochemistry of the core sediment. Water (Switzerland) 15 (10). https://doi.org/10.3390/w15101926.

Tamehe, L.S., Li, H., Ganno, S., Chen, Z., Lemdjou, Y.B., Elatikpo, S.M., 2024. Insight into the origin of iron ore based on elemental contents of magnetite and whole-rock geochemistry: a case of the bipindi banded iron formations, nyong complex, SW Cameroon. J. Earth Sci. 35 (1), 16–28. https://doi.org/10.1007/s12583-022-1622-4.

Tsangaratos, P., Vakalas, I., Zanarini, I., 2025. Distinguishing lithofacies of flysch formations using deep learning models: integrating remote sensing data with morphological indexes. Remote Sens. 17 (3), 422. https://doi.org/10.3390/rs17030422.

Ullah, J., Li, H., Abdalla, R.M., Asad, M., Tai, A.P.K., Falaknaz, A., 2025a. Optimizing support vector machines for enhanced permeability prediction in sandstone reservoirs using systematic and heuristic hyperparameter tuning. Earth Science Informatics 18 (1), 88. https://doi.org/10.1007/s12145-024-01581-3.

Ullah, J., Li, H., Ashraf, U., Heping, P., Ali, M., Ehsan, M., Asad, M., Anees, A., Ren, T., 2023. Knowledge-based machine learning for mineral classification in a complex tectonic regime of Yingxiu-Beichuan fault zone, Sichuan basin. Geoenergy Sci. Eng. 229, 212077. https://doi.org/10.1016/j.geoen.2023.212077.

Ullah, J., Li, H., Soupios, P., Ehsan, M., 2024. Optimizing geothermal reservoir modeling: a unified bayesian PSO and BiGRU approach for precise history matching under uncertainty. Geothermics 119, 102958. https://doi.org/10.1016/j.geothermics.2024.102958.

Ullah, J., Li, H., Yinhui, Z., Ehsan, M., Soupios, P., 2025b. Enhancing reservoir characterization: genetic algorithm-assisted correction of Pore aspect ratio using CNN-LSTM in petrophysical modeling. IEEE Trans. Geosci. Rem. Sens. 63, 1–11. https://doi.org/10.1109/TGRS.2025.3548650.

Vail, J.R., 1990. Geochronology of the Sudan. H.M. Stationery Office, Issue 66 of Overseas geology and mineral resources. https://books.google.hu/books?id=_mu7zQEACAAJ.

Van der Meer, F.D., van der Werff, H.M.A., van Ruitenbeek, F.J.A., 2014. Potential of ESA's Sentinel-2 for geological applications. Rem. Sens. Environ. 148, 124–133. https://doi.org/10.1016/j.rse.2014.03.022.

van der Meer, F.D., van der Werff, H.M.A., van Ruitenbeek, F.J.A., Hecker, C.A., Bakker, W.H., Noomen, M.F., van der Meijde, M., Carranza, E.J.M., de Smeth, J.B., Woldai, T., 2012. Multi- and hyperspectral geologic remote sensing: a review. Int. J. Appl. Earth Obs. Geoinf. 14 (1), 112–128. https://doi.org/10.1016/j.jag.2011.08.002. Elsevier B.V.

van der Werff, H., van der Meer, F., 2015. Sentinel-2 for mapping iron absorption feature parameters. Remote Sens. 7 (10), 12635–12653. https://doi.org/10.3390/rs71012635.

Vapnik, V.N., 1995. The Nature of Statistical Learning Theory. Springer, New York. https://doi.org/10.1007/978-1-4757-2440-0.

Velasco, F., Alvaro, A., Suarez, S., Herrero, J.M., Yusta, I., 2005. Mapping Fe-bearing hydrated sulphate minerals with short wave infrared (SWIR) spectral analysis at San Miguel mine environment, Iberian Pyrite Belt (SW Spain). J. Geochem. Explor. 87 (2), 45–72. https://doi.org/10.1016/j.gexplo.2005.07.002.

Verbovšek, T., Popit, T., 2018. GIS-assisted classification of litho-geomorphological units using Maximum Likelihood Classification, Vipava Valley, SW Slovenia. Landslides 15 (7), 1415–1424. https://doi.org/10.1007/s10346-018-1004-2.

Wilamowski, B., 2009. Neural network architectures and learning algorithms. IEEE Industrial Electronics Magazine 3 (4), 56–63. https://doi.org/10.1109/MIE.2009.934790.

Zhang, X., Pazner, M., Duke, N., 2007. Lithologic and mineral information extraction for gold exploration using ASTER data in the south Chocolate Mountains (California). ISPRS J. Photogrammetry Remote Sens. 62 (4), 271–282. https://doi.org/10.1016/j.isprsjprs.2007.04.004.

Zhang, Z., Yin, F., Zhu, Y., Liu, L., 2025. Lithologic mapping in the Karamaili ophiolite–mélange Belt in Xinjiang, China, with machine learning and integration of SDGSAT-1 TIS, Landsat-8 OLI and ASTER-GDEM. Nat. Resour. Res. https://doi.org/10.1007/s11053-025-10467-0.